doi:10.26443/seismica.v4i1.1413

The InSAR lookbook: an illustrated guide to earthquake deformation interferograms

Israporn Sethanant *[1,2], **Edwin Nissen** [1,3]

[1]School of Earth and Ocean Sciences, University of Victoria, Victoria BC, Canada, [2]School of Geography, Earth and Atmospheric Sciences, The University of Melbourne, Victoria, Australia, [3]College of Earth, Ocean and Atmospheric Sciences, Oregon State University, Corvallis, Oregon, USA

Author contributions: *Conceptualization*: I.S., E.N.. *Formal Analysis*: I.S.. *Investigation*: I.S., E.N.. *Writing - Original draft*: I.S.. *Writing - Review & Editing*: E.N.. *Visualization*: I.S.. *Supervision*: E.N..

Abstract Satellite-borne Interferometric Synthetic Aperture Radar (InSAR) is the prevalent method for mapping earthquake land-surface deformation and is seeing ever-increasing popularity through a new generation of satellite missions. Nowadays, following any large onshore or nearshore earthquake, InSAR images (interferograms) are quickly disseminated across the scientific community and media. However, interpreting interferograms remains unintuitive, owing to the distinctive way the direction of ground deformation is convolved with effects of satellite viewing geometry. The aim of this paper is to provide a one-stop guide to this interpretation. We begin by describing how InSAR fringe patterns are determined by the combination of horizontal and vertical ground displacements and the look directions from ascending or descending satellite orbits. We then synthesize interferograms for a comprehensive suite of strike-slip, reverse/thrust, normal, and oblique-slip faulting styles. This "lookbook" highlights the most common InSAR fringe patterns and demonstrates visually how strike-slip, dip-slip, and oblique-slip earthquakes produce distinct fringe patterns controlled by their strike angles. We offer guidelines for utilizing the lookbook to estimate focal mechanisms from real earthquake deformation interferograms and pick the causative fault plane from two nodal planes. Lastly, we showcase the applicability of the lookbook through comparisons with real-world earthquake deformation interferograms.

Handling Editor:
Wenbin Xu
Copy & Layout Editor:
Miguel Neves

Signed reviewer(s):
Austin Elliott
John Elliott

Received:
17 July 2024
Accepted:
26 March 2025
Published:
23 April 2025

Non-technical summary Interferometric Synthetic Aperture Radar (InSAR) technology makes use of repeat satellite radar images to map shifts in the ground surface, such as those caused by earthquakes. With some basic guidelines, both the location and style of faulting can quickly be inferred from these images, called interferograms. In this study, we explain the link between three-dimensional earthquake displacements and the patterns seen in the interferograms. We then produce a "lookbook" of model interferograms that showcases the range of deformation patterns characteristic of earthquakes of different fault styles and orientations. For example, faults that slide sideways generate patterns resembling butterfly wings or four-leaf clovers, while those that involve angled thrusting or stretching produce rounded double or triple deformation lobes. Our lookbook can be used to characterize real-world earthquakes quickly, without the need for specialized modelling. This can be useful for earthquake rapid response and can also serve as an effective communication and learning tool for the public and scientific community.

1 Motivation

Since its initial, widespread application in the early 1990s (Gabriel et al., 1989; Massonnet et al., 1993), satellite-borne Interferometric Synthetic Aperture Radar (InSAR) has become the prevalent method for mapping surface deformation in large, onshore earthquakes as well as near-shore subduction-related events. With a new generation of satellites collecting increasingly large volumes of data (Elliott et al., 2015) and web portals such as LiCSAR (Lazecký et al., 2020; Watson et al., 2023), the Alaska Satellite Facility (Kennedy et al., 2021; Meyer et al., 2017), and the Jet Propulsion Laboratory (The Rapid Imaging and Analysis Project; e.g., Owen et al., 2017) processing and releasing much of this imagery automatically, the technique is seeing ever growing popularity and interest. After any notable, modern day earthquake, InSAR deformation maps are quickly shared amongst earthquake scientists, provided to geologists and structural engineers collecting perishable data in the field, and disseminated among the broader geoscience community and general public through media and social media platforms (Watson et al., 2023; Meyer et al., 2017; Xu et al., 2020; Barnhart et al., 2019).

Earthquakes involve the abrupt release of stored, elastic strain through slip along a fault plane, generating significant ground displacement up to about two fault lengths away from the earthquake. To a trained eye, deformation patterns captured by InSAR are therefore indicative of both the rupture location and mechanism. These data are routinely inverted using elastic dislocation models in order to estimate the causative fault plane geometries and slip distributions (e.g., Wright et al., 2013; Mai and Thingbaijam, 2014), eliminating the multi-kilometer location biases and nodal plane ambiguities inherent in most seismic waveform-based

*Corresponding author: israporn.sethanant@unimelb.edu.au

source solutions (Weston et al., 2011, 2012). These refined fault locations can be matched to features expressed in the geomorphology or geology, helping reveal connections between individual earthquakes and large scale topography (e.g., Wright et al., 1999). InSAR fault models provide unparalleled sensitivity to the distribution of slip with depth, vital for understanding shallow slip deficits and off-fault deformation (e.g., Fialko et al., 2005; Dolan and Haravitch, 2014; Sethanant et al., 2023). They can also help characterize multi-segment earthquakes to a degree that is impossible from seismic data alone, helping constrain the processes of rupture propagation and arrest (e.g., Nissen et al., 2016; Hamling et al., 2017). Consequently, InSAR modelling studies have greatly enhanced our understanding of both active tectonics and earthquake physics. Furthermore, interferograms can capture important secondary earthquake effects including surface fracturing or bedding plane slip, landsliding, liquefaction, and even building collapse (e.g., Fielding et al., 2005; Ishitsuka et al., 2012; Nissen et al., 2016; Huang et al., 2017; Xu et al., 2020). However, to our knowledge there is not yet a singular, comprehensive quick-reference guide on how to "read" interferograms. Even for InSAR specialists, certain types of earthquakes at particular strike angles can produce complicated signals that are difficult to understand at first glance.

The aim of this study is to provide an illustrated guide to interpreting InSAR signals through a comprehensive suite of model interferograms spanning a wide range of fault types and orientations. Our work builds upon an earlier, interactive, web-based tool for simulating interferograms, called "Visible Earthquakes" (Funning and Cockett, 2012), now discontinued. In Section 2, we briefly introduce InSAR before using an elastic dislocation model to illustrate how 3-D earthquake deformation is resolved into the line-of-sight (LOS) displacements to which InSAR is sensitive, a vital concept for understanding why InSAR signals look the way they do. Here, we assume the right-side looking SAR antenna geometries prevalent amongst non-commercial, near-polar orbiting satellite platforms, and we do not further discuss emergent airborne platforms that allow for much greater flexibility in look angles (Delbridge et al., 2016). In Section 3, we describe our forward modelling set-up for the lookbook itself, presented in Section 4. The lookbook captures end-member faulting styles including left- and right-lateral strike-slip (Section 4.1), moderate angle reverse and normal faulting (Section 4.2), low-angle thrust and normal slip (Section 4.3), as well as steep- and gentle-angle oblique-slip mechanisms (Section 4.4). For each fault type, interferograms are arranged radially by fault strike (and later, rake) such that the reader can visually assess its influence on the observed InSAR fringe patterns. Finally, in Section 5, we show how this lookbook can help assess real-world earthquakes using a number of recent examples.

2 A brief introduction to InSAR and co-seismic interferograms

2.1 How InSAR works

Here we provide a brief overview of how InSAR works, directing readers to Massonnet and Feigl (1998), Bürgmann et al. (2000), Rosen et al. (2000), and Elliott et al. (2016) for more comprehensive reviews. Synthetic Aperture Radar (SAR) satellites deploy side-looking radio detection and ranging (radar) antennae that illuminate the Earth with electromagnetic signals, usually in the X-band (2.5–3.75 cm), C-band (3.75–7.5 cm), S-band (7.5–15 cm), or L-band (15–30 cm) of the radio spectrum (Institute of Electrical and Electronics Engineers, 2020), and record the amplitude and phase of back-scattered energy (Figure 1). The synthetic aperture refers to the simulation of an extremely long antenna by combining successive radar returns along the satellite orbital path, greatly improving pixel resolution within the image (Bürgmann et al., 2000) (Figure 1c). To date, most non-commercial Earth observation SAR missions have deployed right side-looking antennae on satellites in low Earth (∼800 km altitude), sun-synchronous, near-polar orbits (inclination ∼97–99°). This configuration gives rise to LOS vectors pointing just north of eastward on ascending orbital tracks and just north of westward on descending ones (Figure 1a, b), deviating significantly only where the satellites approach either pole. LOS incidence angles measured from the vertical range from ∼20–45°, depending on the satellite.

Repeat-pass Interferometric SAR (InSAR) uses successive phase images collected from approximately the same position but at different times. Minimum revisit times are 4–6 days for newer, multi-satellite missions such as the Canadian Space Agency's RADARSAT Constellation Mission and the European Space Agency's Sentinel-1 pair, and 35–46 days for older, single-satellite missions such as ERS-1, ERS-2, ENVISAT, ALOS-1, and ALOS-2. However, due to power limitations, SAR images are not acquired on every pass. Following an earthquake of interest, the temporal baseline will depend on the timings of the last pre-seismic image acquisition and the next satellite pass. For older satellites, temporal baselines of several months were common.

Though a single phase image is effectively random, differencing a pair of images creates a meaningful interference pattern (called an interferogram) which captures the spatial distribution of changes in the distance traveled by the radar pulse. The phase change for an individual pixel in an interferogram reflects several factors. These include (1) the difference in antenna position between the two image acquisitions as measured perpendicular to viewing direction, known as the perpendicular baseline and typically in the range ∼100–1000 m; (2) a resulting, perspective effect of Earth's topography; (3) atmospheric path delays from free electrons in the ionosphere and water vapour in the troposphere; and (4) any Earth surface deformation towards or away from the satellite. The first two of these phase contributions are straightforward to account for using precise orbital information and topo-

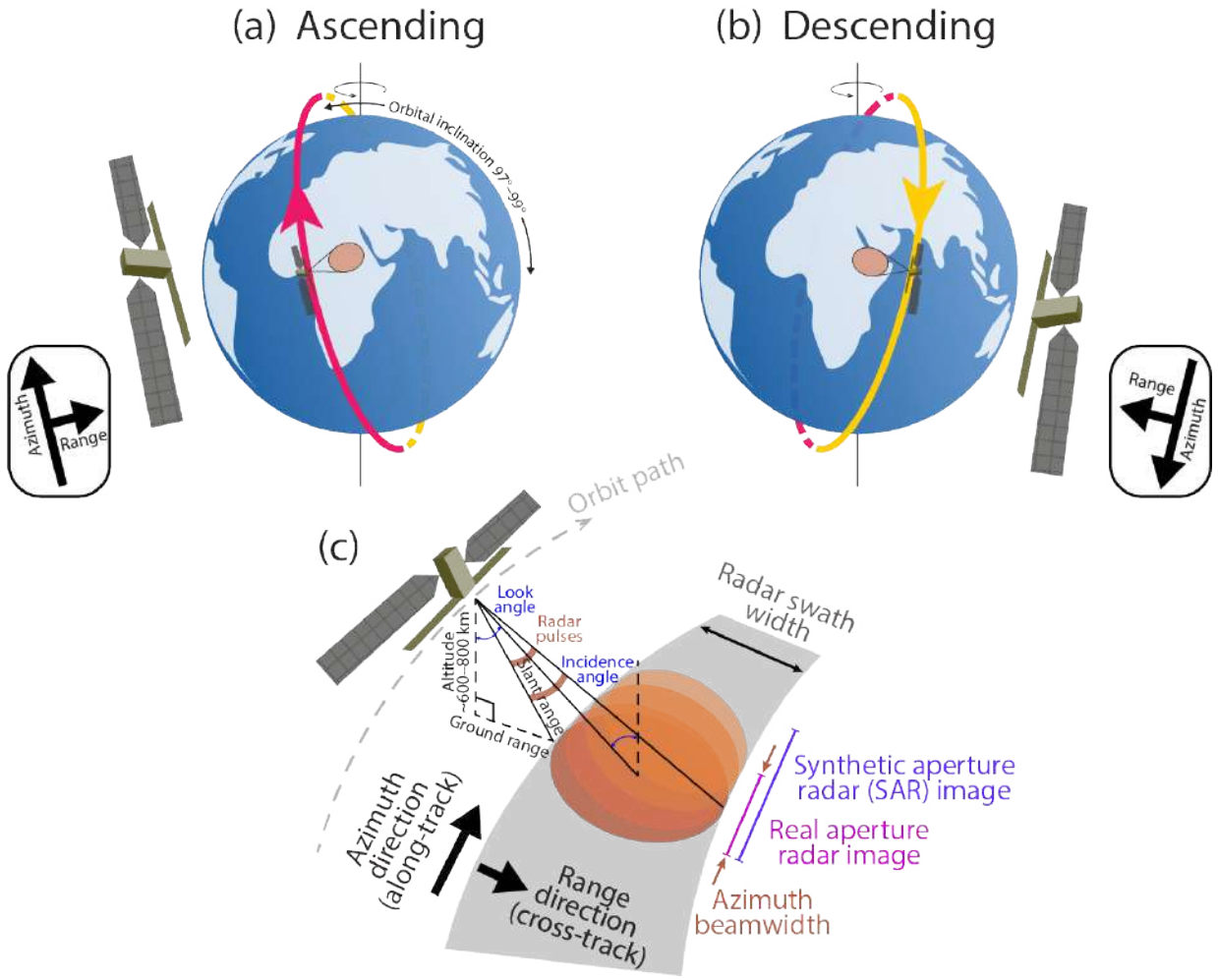

Figure 1 Schematic illustration of (a) ascending and (b) descending near-polar, sun-synchronous satellite orbits, showing the right-side looking synthetic aperture radar system prevalent amongst established non-commercial missions. (c) Acquisition geometry showing footprints of real aperture and Synthetic Aperture Radar (SAR) images. Conjugate thick arrows denote the azimuth and range directions.

graphic corrections, and the third can be mitigated using atmospheric models (Yu et al., 2018). This leaves mostly ground deformation, typically resolvable from residual atmospheric noise at the centimetric level. However, the coherence of an interferogram also relies on pixel back-scattering characteristics remaining unchanged between two images. Growing vegetation, agriculture, snow cover, flooding, and effects related to large earthquakes including surface rupturing, liquefaction, landsliding, building collapse, and even the strong ground accelerations themselves, can all cause interferograms to decorrelate (e.g., Rosen et al., 2000; Zebker and Villasenor, 1992). Moreover, decorrelation occurs whenever the phase gradient exceeds a half-radar-wavelength per pixel. This can occur in steep, mountainous topography due to the close spacing of topographic fringes, as well as amidst zones of high strain, which in the case of earthquakes are most commonly found around the causative fault and in particular any surface rupture traces. In these cases, other remote sensing techniques such as optical image correlation and differential lidar can be used to map near-field displacements, measure fault offsets, and improve the resolution of slip models at shallow depths (e.g., Milliner et al., 2015; Scott et al., 2019; Gaudreau et al., 2023).

InSAR signals are conventionally displayed as color cycles, or "fringes", each representing a contour of one half-radar-wavelength of LOS displacement, with the order of color change indicating whether ground displacement is towards or away from the satellite. As long as the data are available, deformation associated with the earthquakes of interest will always be mapped from both ascending and descending orbital tracks, providing two independent look angles (Figure 1a, b). Whatever the orbital track, uplift and subsidence will produce motion towards and away from the satellite, respectively, whereas eastward and westward ground displacements will be resolved oppositely in ascending and descending interferograms. Much like elevation contours on a topographic map, closely-spaced and compact fringes indicate steeper LOS displacement gradients, while wider fringes reflect gentler or absent deformation. Fringes can also be added up into a map of cumulative LOS displacement, a process called phase unwrapping (Massonnet and Feigl, 1998; Zebker and Lu, 1998), though doing so can introduce errors, particularly in regions of partial decorrelation. Moreover, deformation is often easiest to visualize with the fringe

contouring of the original (wrapped) interferograms.

The detectability of earthquakes in InSAR imagery is conditioned upon fault slip being large and shallow enough that surface deformation exceeds atmospheric noise, which is typically up to a few centimeters in amplitude. A good rule of thumb is that events with moment magnitudes (M_w) greater than ~6 and at depths less than ~10 km are usually detectable unless the imagery is badly compromised by phase decorrelation (Funning and Garcia, 2019). However, important second order features of the surface deformation pattern—for example small fringe lobes at fault tips and drawn out fringe lobes in the far-field—may not be resolvable from atmospheric noise until larger magnitudes are realized. Even if a moderate magnitude earthquake is detectable, this limitation can render it difficult to resolve important source parameters such as fault length, dip, and bottom depth.

2.2 Why coseismic interferograms look as they do

Next, we use a simple elastic dislocation model (e.g., Wright et al., 1999) to demonstrate how 3-D coseismic displacements map into satellite LOS displacements at different orientations. In this section, we follow a similar line of reasoning to that used by Funning et al. (2005) to explain fringe patterns in the 2003 Bam, Iran earthquake. We use the same modelling set-up as for the main lookbook (described in Section 3) with the left-lateral strike-slip and moderately-dipping (45°) normal fault parameters from Table 1. A 45°-dipping reverse faulting earthquake would generate the same deformation pattern as the normal faulting earthquake, except with the exact opposite horizontal and vertical displacement sense.

2.2.1 Strike-slip earthquakes

In Figure 2a (left panel), we plot the theoretical 3-D displacement field for a surface-rupturing, N-trending and vertically-dipping left-lateral strike-slip earthquake (Table 1). Horizontal displacement vectors are plotted at regular intervals over a color map of vertical displacement, with red indicating uplift and blue subsidence. In the near field, horizontal displacement vectors are longest, and parallel to the fault, on either side of the fault center, while they are shorter, and at oblique angles, around the fault tips. Horizontal displacement vectors also shorten with increasing distance from the fault, in every direction. Vertical displacements for a strike-slip fault are small, but non-negligible, especially around the fault endpoints where horizontal contraction and extension results in uplift and subsidence, respectively. SW and NE of the fault trace, horizontal displacement vectors are shortening, explaining the two regions of uplift, whereas NW and SE of it, vectors are lengthening, leading to stretching and subsidence. The sense of vertical displacement is therefore anti-symmetric both along the fault and perpendicular to it.

In Figure 2a (center and right panels), we separate the horizontal displacement vectors into their distinct N–S and E–W components, still superimposing these onto the vertical deformation color map. The large, lateral displacements parallel to the strike-slip fault are captured in the N–S displacement field (Figure 2a, center panel) while the smaller motions perpendicular to the fault are captured in the E–W displacement field (Figure 2a, right panel). Since InSAR satellites follow near polar orbital tracks and look downwards and to the right, they have very little sensitivity to the N–S displacements (the vectors in the center panel), but much stronger sensitivity to both the E–W and vertical displacements (Figure 2a, right panel).

In an ascending track interferogram, the InSAR look vector is roughly equal parts towards the ENE and downwards (Figure 2b, top panels). The NW quadrant of the displacement field thus comprises motions that are horizontally away (eastward) and vertically away (downward) from the satellite, adding constructively into a strong LOS displacement away from the satellite (Figure 2b, top left) and resulting in densely packed fringes in the wrapped interferogram (Figure 2b, top right). In the NE quadrant, displacements are horizontally away (eastward) but vertically towards (upward) the satellite, partially cancelling out for a weaker LOS displacement away from the satellite and fewer fringes. In the SW quadrant, westward and upward displacement combines into a strong LOS displacement towards the satellite, while in the SE quadrant the westward and downward motions partially cancel each other out for a weak LOS displacement towards the satellite. Thus, the combinations of E–W and vertical motions in the four quadrants of the ascending interferogram produce two northern deformation lobes with motion away from the satellite and two southern lobes with motion towards the satellite, with stronger LOS displacements and more densely packed fringes in the western lobes and weaker LOS displacements with fewer fringes in the eastern ones (Figure 2b, top right).

On its descending track, the satellite observes the same displacement field differently, looking in roughly equal parts to the WNW and downwards (Figure 2b, bottom panels). In the NW quadrant, motions are horizontally towards (eastward) but vertically away (downward) from the satellite, partially cancelling out (Figure 2b, bottom left). In the NE quadrant, displacements are horizontally towards (eastward) and vertically towards (upward) the satellite, adding to strong LOS displacements towards the satellite. Likewise, motions in the SW quadrant partially cancel out, while those in the SE quadrant constructively interfere to generate strong LOS displacement away from the satellite. Therefore, the descending interferogram also generates two lobes each of motion towards and away from the satellite, but this time LOS displacements are strongest and fringes most densely packed on the eastern side of the fault (Figure 2b, bottom right), opposite to the ascending interferogram.

Next, we repeat the exercise for an E–W-trending left-lateral strike-slip earthquake. The 3-D displacement field is the same as for the N–S earthquake, but rotated 90° (Figure 2c). The large, lateral displacements parallel to the strike-slip fault are now captured in the E–

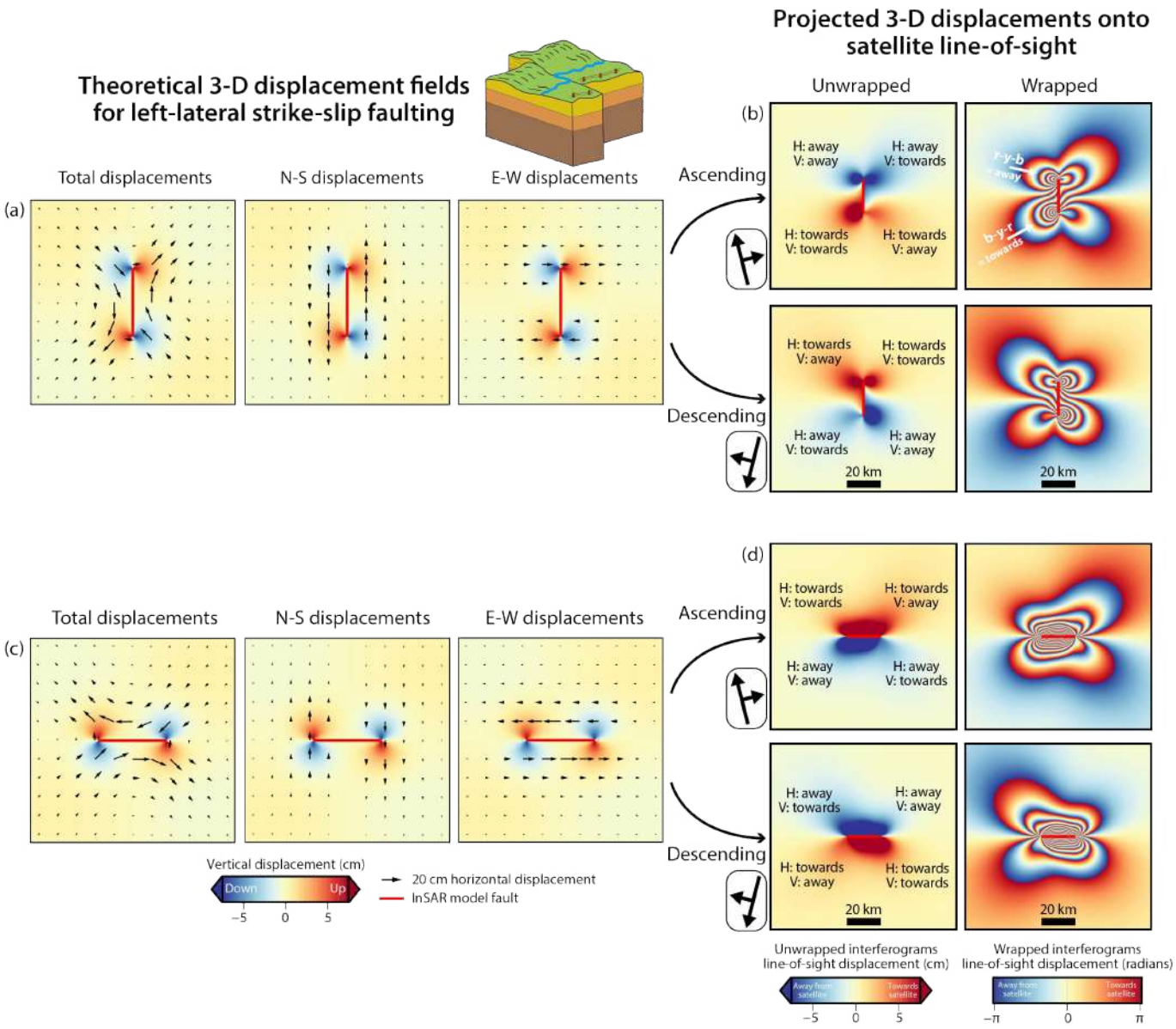

Figure 2 (Left) 3-D displacement fields and (right) unwrapped and wrapped interferograms for a (a, b) N–S-oriented and (c, d) E–W-oriented vertically-dipping left-lateral strike-slip earthquake along the fault outlined in red. On the left side of the figure (a, c), horizontal motions (black vectors) are overlain on a color map of vertical displacement (red is uplift and blue subsidence). The left panels shows full horizontal displacements while the center and right panels split these into their N-S and E-W components, respectively. On the right side of the figure (b, d), the 3-D displacements are projected onto the satellite LOS to produce (top) ascending and (bottom) descending (left) unwrapped and (right) wrapped interferograms. As is convention, satellite geometries are denoted by conjugate arrows, with the long arrows indicating satellite azimuths and the short one indicating horizontal components of the LOS vector. Across the ascending scene, LOS unit vectors (pointing from the pixel on the ground to the satellite) have east, north, and up components ranging from −0.67 to −0.54, −0.12 to −0.09, and 0.73 to 0.84, respectively. Across the descending scene, the equivalent ranges are 0.53 to 0.67, −0.13 to −0.10, and 0.73 to 0.84. Annotations in the unwrapped interferograms denote the horizontal (H) and vertical (V) components of LOS displacement. White arrows illustrate color cycle order from blue (b) to yellow (y) to red (r), indicating motion towards the satellite, and vice versa (see Section 3.1 for displacement sense convention).

W displacement field (Figure 2c, right panel), to which InSAR is highly sensitive, whereas the smaller fault-perpendicular motions are captured in the N–S displacement field (Figure 2c, center panel), to which InSAR is mostly insensitive. In the ascending track interferogram, the strong westward motion N of the fault interferes constructively with uplift in the NW quadrant but destructively with subsidence in the NE quadrant, merging into a single, lopsided lobe with LOS displacement towards the satellite (Figure 2d, top panels). Similar interference on the S side of the fault, where eastward lateral motion dominates, results in a single, lopsided lobe containing LOS displacement away from the satellite. There are therefore two deformation lobes, towards the satellite in the North and away from it in the South (Figure 2d, top left), with the densest fringes in the west and the longest wavelengths in the east, appearing to "skew" the fringe patterns in this direction

(Figure 2d, top right). Following the same reasoning, the descending track interferogram is a double mirror image of the ascending one, with single northern and southern lobes containing displacement away from and towards the satellite, respectively, both skewed westwards (Figure 2d, bottom panels). This demonstrates an important point: that asymmetric lobe shapes often simply reflect InSAR look geometries, rather than variations in slip along strike as might seem intuitive.

2.2.2 Dip-slip earthquakes

The 3-D displacement field for a N-striking normal faulting earthquake is dominated by vertical subsidence in the hanging wall east of the fault, with a much smaller amount of uplift in the footwall west of it (Figure 3a, left panel). Horizontal displacements are greatest either side of the fault center, where they are perpendicular to the fault, and smaller towards the fault tips, where they include increasing fault-parallel components, pointing radially outwards west of the fault and inwards east of it. The E–W displacement field, to which InSAR is sensitive, captures the large, fault-perpendicular displacements (Figure 3a, right panel), while the N–S displacements, to which InSAR is insensitive, includes the smaller fault-parallel motions (Figure 3a, center panel).

In the near-field of the hanging wall east of the fault, LOS displacements are dominated by subsidence, leading to motion away from the satellite in both ascending and descending interferograms (Figure 3b, left panels). The deformation lobe is narrow, with closely packed fringes in the wrapped interferograms centered directly above the eastward-dipping fault plane (Figure 3b, right panels). Further east, far-field displacements comprise eastward motions that are away from the ascending satellite and towards descending one (Figure 3b, left panels). In the ascending interferogram, the near- and far-field hanging wall lobes are both negative, thus merging together, whereas in the descending interferogram they are of opposite displacement sense, staying as separate near-field negative and far-field positive lobes. In the footwall west of the fault, both interferograms are dominated by fault perpendicular westward motion, forming a single deformation lobe moving towards the ascending satellite but away from the descending one. Overall, the ascending interferogram thus contains two distinct lobes, and the descending interferogram three.

For an E-striking normal faulting earthquake, the large, lateral displacements perpendicular to the normal fault are now captured in the N–S displacement field, to which InSAR is mostly insensitive, whereas the smaller fault-parallel motions are captured in the E–W displacement field, which the InSAR picks up (Figure 3c). Near-field LOS displacements in the hanging wall south of the fault are still dominated by vertical motion away from the satellite, resulting in a narrow lobe centered above the dipping fault in both the ascending and descending interferograms (Figure 3d). In the footwall north of the fault, LOS deformation mostly reflects the smaller, fault-parallel motions around the fault tips. These result in an arrangement of smaller lobes (three positive, one negative) surrounding the dense, central lobe in both interferograms, which are mirror images of one another about the N–S axis. Interferograms of reverse faulting earthquakes would have the same arrangement but of opposite sense, with three negative lobes and one positive lobe surrounding the dense, central fringes.

3 Introducing the InSAR lookbook

3.1 Model set-up and displacement sense convention

We used the formulae of Okada (1985) implemented in Oksar software (Wright et al., 1999) to generate displacement fields for earthquakes represented as uniform slip on planar, rectangular dislocations embedded in an elastic half-space with Lamé parameters λ and μ of 3.2×10^{10} Pa. For each earthquake configuration (described below), 3-dimensional surface displacements were mapped across a 150 km $\times$ 150 km region at a 100 m spatial resolution. These were then projected into the ascending and descending satellite line-of-sight, using a local Earth radius of 6,370 km, a satellite height of 700 km, and satellite azimuths of 350.1° (ascending) and 190.7° (descending). These parameters are based upon European Space Agency Sentinel-1 orbits at mid latitudes, and we chose a center scene incidence angle of 38.3°, equivalent to the middle of a Sentinel-1 Interferometric Wide Swath scene at the same latitude (European Space Agency). Incidence angles along the edges of Sentinel-1's wide swath differ by $\pm$7–8° from those at the center, which for the purposes of our lookbook would give rise to only subtle changes in the model interferograms (though we recognize that for earthquakes rupturing across large InSAR footprints, it is still important to account for these variations). Finally, we wrapped the LOS displacements using the Sentinel-1 half-wavelength of 2.77 cm.

There is currently no settled consensus amongst the InSAR community on how to represent the sense of ground displacement in interferograms (whether towards or away from the satellite), and so we first establish our own convention and terminology. For unwrapped interferograms, we use red and blue colors to refer to motion towards and away from the satellite, respectively; this seems intuitive to most geologists and is the common convention in the seismology literature. For wrapped interferograms, it is easiest to think first of the far-field deformation as approximating zero, and then to consider the color order as one approaches the earthquake signal from any one side of it. Here, we use the convention that when crossing fringes in the order blue through yellow to red (abbreviated as blue–yellow–red or b–y–r), motion is increasingly towards the satellite. For simplicity and brevity, we call these fringes "positive lobes". If, approaching the fault, the colors instead cycle red–yellow–blue (r–y–b), then motions are increasingly away from the satellite, and we call the region a "negative lobe".

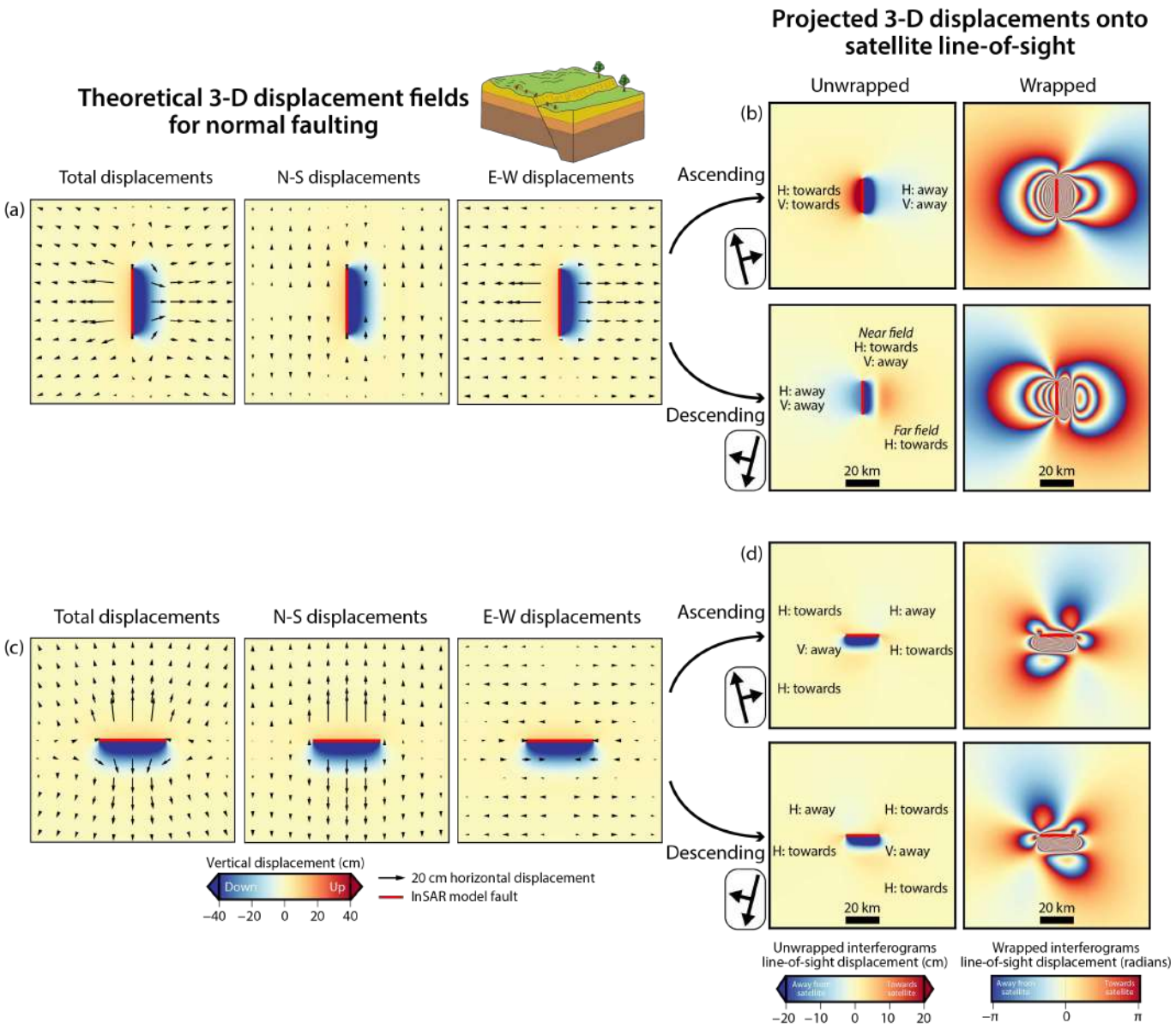

Figure 3 (Left) 3-D displacement fields and (right) unwrapped and wrapped interferograms for a (a, b) N-striking (E-dipping) and (c, d) E-striking (S-dipping) normal faulting earthquake (surface trace in red). On the left side of the figure (a, c), horizontal motions (black vectors) are overlain on a color map of vertical displacement (red is uplift and blue subsidence). The left panels shows full horizontal displacements while the center and right panels split these into their N-S and E-W components, respectively. On the right side of the figure (b, d), the 3-D displacements are projected onto the satellite LOS to produce (top) ascending and (bottom) descending (left) unwrapped and (right) wrapped interferograms. As is convention, satellite geometries are denoted by conjugate arrows, with the long arrows indicating satellite azimuths and the short one indicating horizontal components of the LOS vector. LOS unit vectors are as listed in the Figure 2 caption. Annotations in the unwrapped interferograms denote the horizontal (H) and vertical (V) components of LOS displacement.

3.2 Model fault configurations

We forward modelled fourteen types of earthquake at each of twelve different strike orientations, at 30° increments from 0° to 330°. For each configuration, we produced four interferograms: ascending and descending, wrapped and unwrapped. The fourteen faulting types incorporate rake values of 0° and 180° for vertical strike-slip earthquakes, 90° and −90° dip-slip (reverse/thrust and normal faulting) earthquakes in each of moderate- and low-angle orientations, and 45°, 135°, −135° and −45° for oblique-slip earthquakes in each of steep-angle and gentle-angle orientations (Table 1). The moderate-angle reverse and normal faulting earthquakes dip at 45°, based on a global survey of continental dip-slip focal mechanisms (Middleton and Copley, 2013; Collettini and Sibson, 2001). The low-angle thrust and normal earthquakes dip at 10°, signifying slip on sub-horizontal décollements or detachments. The steep- and gentle-angle oblique-slip earthquakes dip at 67.5° and 22.5°, respectively—in other words midway between moderate-angle and vertical or horizontal. In all cases, we used a 20 km-long and 10 km-wide fault plane with uniform slip of 1 m for consistency with fault length scaling relationships (Wells and Coppersmith, 1994), yielding a seismic moment of 6.4×10^{18} Nm,

equivalent to a moment magnitude (M_w) of 6.5. For most earthquake types, the fault top depth is zero; the fault bottom depths therefore differ according to dip angle, but the length to width ratio is a constant 2 to 1 (Table 1). The exceptions are our low-angle thrust and low-angle normal faulting earthquakes, centered at just below 10 km depth to mimic slip on décollements or detachments.

3.3 How to use the lookbook

The overarching goal of the lookbook is to help readers interpret real coseismic interferograms. When InSAR imagery of an earthquake become available, users can match them with model interferograms plotted in the lookbook to make a first order interpretation or estimation of the rupture mechanism.

We provide Table 1 to help the reader navigate to the appropriate figure within the lookbook. Two types of figures are listed. In the top half of the table, there is a figure for each fixed style of faulting, in which ascending/descending interferogram pairs are plotted radially at 30° increments of strike (Figures 4–17; equivalent unwrapped interferograms are provided in Supplementary Figures S1a–S1n). This type of figure will be most useful when the style of faulting is either known (for example, from an independent seismological focal mechanism, such as those often made available well before the first InSAR imagery by earthquake monitoring centers), or suspected (for example, using knowledge of the tectonic setting). Often, this will help narrow the search for the relevant InSAR signal in the lookbook to one of two possibilities, representing each nodal plane. The lookbook may then help users distinguish the fault plane from the auxiliary plane of the focal mechanism (though even with InSAR imagery to hand, there is sometimes still a nodal plane ambiguity if the rupture does not reach the surface).

In the bottom half of Table 1, there is a figure for each fixed orientation of fault strike, in which ascending/descending pairs of wrapped interferograms are plotted radially at 45° increments of rake (Figures S2a–S2l). These figures are more appropriate for when the style of faulting is unknown, but they do require an estimation of the fault strike. Often, the strike can be estimated directly from the interferogram, using any observed displacement discontinuity or linear zone of image decorrelation, such as are expected along earthquake surface ruptures.

3.4 Extrapolating and interpolating the lookbook models

Naturally, the model earthquakes in the lookbook represent a tiny fraction of all source parameter space, and ultimately inverse models are needed to determine the best-fitting fault geometry and slip distribution. Readers should therefore use the lookbook models only as first order approximations of real interferograms. However, equipped with a feel for how each variable impacts the deformation field, they can also interpolate or extrapolate the lookbook model faults to approximate the source parameters of a real earthquake from a set of observed interferograms.

For example, earthquake ruptures striking at 10° or 20° will generate fringe patterns roughly intermediate to those of our 0°- and 30°-striking forward models. Variations in dip or rake away from our fixed series of values will skew the relative amplitudes and/or positioning of InSAR deformation lobes, without changing the essential pattern. Similarly, extending the bottom of the fault to greater depths will increase far-field displacements without impacting those along the fault trace. Lengthening the fault stretches the fringes in the along-strike direction, without altering those around the fault ends. Fault slip, the only parameter in linear relation to surface deformation, controls the number of fringes but not the pattern; for example, an earthquake with half or double the moment of one of our models will simply half or double the number of fringes. Similarly, wrapped interferograms generated from satellites with longer wavelengths than Sentinel-1 (e.g., ALOS-2) will have fewer fringes than our forward models, but will retain the same shape.

We illustrate some of these effects with explicit sensitivity tests for two of the most important source parameters, fault dip angle and burial depth. Figure 18 shows a series of interferograms for N- and E-striking left-lateral and normal faults with varying dip angles. In general, the dip angle is seen to control the balance of fringes on either side of the fault surface trace. Figure 19 shows a similar series of interferograms with varying fault burial depths. Burying the top of the fault acts to smooth out the sharp LOS displacement discontinuity along the projected fault surface trace, without much impacting the far-field deformation.

3.5 Limitations

Real earthquakes involve variations in slip and rake over the fault surface, which may not be planar. The longest continental ruptures often display multiple slip asperities along strike, giving rise to “string of pearl” InSAR fringe patterns that surpass the simplicity of our lookbook interferograms. A good example of this phenomenon was the 2008 M_w 7.9 Wenchuan, China earthquake, which exhibited at least four discrete patches of multi-meter (∼5–8 m) slip along the ∼250 km-long fault (Tong et al., 2010; Wan et al., 2016). Multi-fault ruptures are a separate class of earthquake involving near-simultaneous failure of more than one discrete fault, and naturally cannot be modelled closely using a single dislocation. Notable examples include the 2010 M_w 7.1 Darfield and 2016 M_w 7.8 Kaikoura earthquakes, both in New Zealand, the 2010 M_w 7.2 El Mayor-Cucapah earthquake in Mexico, and the 2019 M_w 7.1 Ridgecrest earthquake in California. To fit InSAR data closely, published models of these earthquakes incorporate several discrete fault segments with widely variable geometries and kinematics (Elliott et al., 2012; Hamling et al., 2017; Wei et al., 2011; Magen et al., 2020). The uniform slip models in our lookbook cannot feasibly capture such complexities, underscoring the importance of modelling source geometries and slip distributions, es-

Table 1 Index listing all suites of model earthquakes presented in the lookbook, their underlying source parameters, and where the model interferograms are plotted; the first figure listed is the (w)rapped interferogram and the second figure is the (u)nwrapped one. All model earthquakes involve 1.0 m of uniform slip on a 20 km-long, 10 km-wide, rectangular, planar fault.

Earthquake descriptor	**Strike**	**Dip**	**Rake**	**Depth** (km)	**Fig.** (w/u)
Left-lateral strike-slip	variable	90°	0°	0–10	4/S1a
Right-lateral strike-slip	variable	90°	180°	0–10	5/S1b
Reverse	variable	45°	90°	0–7.07	6/S1c
Normal	variable	45°	−90°	0–7.07	7/S1d
Low-angle thrust	variable	10°	90°	10–11.74	8/S1e
Low-angle normal	variable	10°	−90°	10–11.74	9/S1f
Steep left-lateral/reverse oblique-slip	variable	67.5°	45°	0–9.24	10/S1g
Steep right-lateral/reverse oblique-slip	variable	67.5°	135°	0–9.24	11/S1h
Steep left-lateral/normal oblique-slip	variable	67.5°	−45°	0–9.24	12/S1i
Steep right-lateral/normal oblique-slip	variable	67.5°	−135°	0–9.24	13/S1j
Gentle left-lateral/thrust oblique-slip	variable	22.5°	45°	0–3.83	14/S1k
Gentle right-lateral/thrust oblique-slip	variable	22.5°	135°	0–3.83	15/S1l
Gentle left-lateral/normal oblique-slip	variable	22.5°	−45°	0–3.83	16/S1m
Gentle right-lateral/normal oblique-slip	variable	22.5°	−135°	0–3.83	17/S1n
N-striking	0°	variable	variable	variable	S2a
NNE-striking	30°	variable	variable	variable	S2b
ENE-striking	60°	variable	variable	variable	S2c
E-striking	90°	variable	variable	variable	S2d
ESE-striking	120°	variable	variable	variable	S2e
SSE-striking	150°	variable	variable	variable	S2f
S-striking	180°	variable	variable	variable	S2g
SSW-striking	210°	variable	variable	variable	S2h
WSW-striking	240°	variable	variable	variable	S2i
W-striking	270°	variable	variable	variable	S2j
WNW-striking	300°	variable	variable	variable	S2k
NNW-striking	330°	variable	variable	variable	S2l

pecially for the largest events.

However, it is also encouraging to us that coseismic interferograms for many earthquakes up to about M_w 6.5 can be fit quite satisfactorily with simple, rectangular, uniform slip planes (e.g. Wright et al., 1999; Berberian et al., 2001; Talebian et al., 2006). Indeed, doing so remains a routine first stage in InSAR inverse modelling studies, with the second stage (solving for slip and rake distributions) often yielding only marginal differences in modelled surface deformation. Generally these differences are greatest along the fault surface trace, particularly for earthquakes that fail to rupture fully to the surface, introducing a shallow slip deficit (e.g., Xu et al., 2016). For earthquakes with simple slip distributions—where slip is concentrated in a single region and tapers towards the fault ends—the observed fringe patterns tend to align closely with our established uniform slip templates.

Finally, at certain fault geometries, it can be difficult to discriminate the causative fault plane from the conjugate nodal plane using InSAR data. This is very similar to the nodal plane ambiguity in seismological focal mechanisms, and is especially problematic for buried earthquakes **(as demonstrated in Figure 19)** or where near-field deformation is decorrelated in the interferogram (as is often the case for large, shallow earthquakes in steep topography). We will discuss this limitation both as we introduce our lookbook interferograms (Section 4) and again as we examine some real earthquake data (Section 5.2).

4 The InSAR lookbook

4.1 Strike-slip earthquakes

Interferograms for left-lateral and right-lateral strike-slip earthquakes are plotted radially by fault strike in Figures 4–5. Because our model strike-slip faults are vertical, interferograms for strikes 0°–150° are identical to those for strikes 180°–330°, but we include the duplication for consistency with later figures with dipping geometries. The left- and right-lateral interferograms mimic one another, but with the sense of displacement (whether towards or away from the satellite) switched.

As described in Section 2.2.1, strike-slip earthquakes generate the simplest patterns of deformation when oriented E–W. Here, there is a broad, positive deformation lobe on one side of the fault mirrored by a broad, negative lobe on the other side, together giving rise to a distinctive butterfly shape. The ascending and descending interferograms give rise to similar patterns but with fully opposing senses of displacement, a diagnostic characteristic of dominantly strike-slip earthquakes. As the faulting rotates away from E–W to WNW or ENE, the lobes become skewed in opposite directions along strike, with the distortion more pronounced in whichever of the ascending or descending interfer-

ograms looks more obliquely to fault strike. At NNW and NNE orientations, a second, smaller pair of lobes emerges at the opposite fault ends to the larger pair. This four-leaf clover pattern becomes more evident still when the fault strikes N–S, with lobes on one side of the fault broader but of lower amplitude than those on the other, for the reasons explained in Section 2.2.1. The northern two lobes have the same displacement sense as one another, and the southern two lobes are both of the opposite sense. Merging of the northern two lobes across the strike of the fault, and of the southern two lobes, can therefore give rise to far-field fringes that closely resemble those of a conjugate strike-slip fault (for example, compare far-field deformation for the N–S-trending left-lateral earthquake in Figure 4 with that for the E–W-trending right-lateral earthquake in Figure 5). Thus, in the absence of positive identification of fault strike—for example due to decorrelation or fault burial—it can be difficult to discriminate the fault plane from the auxiliary plane for strike-slip earthquakes. This effect is evident in our fault burial depth sensitivity tests (Figure 19), in which strike-slip earthquakes buried to 10 km or 15 km depth are shown to have highly-smoothed fringe patterns. In such cases, additional constraints from slip modelling or from independent seismological data may be needed to ascertain fault strike with confidence (e.g., Biggs et al., 2006).

4.2 Moderate angle dip-slip earthquakes

For reverse and normal faulting earthquakes at moderate dip angles (we use 45° in our models), 3-D deformation fields will comprise roughly equal parts horizontal and vertical displacement. Horizontal deformation is dominated by displacement perpendicular to the fault trace: towards the fault in the reverse case (reflecting shortening) and away from it in the normal case (reflecting extension; see Figure 3a, c). Adjacent to the fault center, horizontal displacement is only towards or away from the fault, while around the fault ends, there are also smaller fault-parallel components. While InSAR will always be sensitive to the vertical component, how much of the horizontal component is also captured will thus depend on the fault orientation, which governs the balance of visible E–W and invisible N–S deformation.

Interferograms for earthquakes involving reverse faulting (rake = 90°) and normal faulting (rake = −90°) are plotted radially by strike in Figures 6–7. These sets of interferograms are exact copies of one another but with the sense of displacement flipped. All of these interferograms exhibit a condensed, central deformation lobe in the hanging wall directly over the dipping fault, in which strong vertical deformation manifests in both ascending and descending interferograms as displacement towards the satellite in the reverse case and displacement away from it in the normal case. In real interferograms, this central area is often substantially decorrelated by the close fringe spacing (e.g., Wright et al., 1999).

The central hanging wall deformation is surrounded by variable numbers of broader, longer wavelength deformation lobes. As described in Section 2.2.2, dip-slip earthquakes at northerly and southerly strikes have the simplest far-field lobe patterns, with two roughly equally-sized lobes extending W and E of the fault in both ascending and descending interferograms. These far-field lobes are dominated by horizontal motion towards the fault in the reverse case (Figure 6) and away from the the fault in the normal case (Figure 7), explaining why they exhibit the opposite displacement sense at ascending and descending viewing angles. For example, for reverse faulting earthquakes, the western lobe is negative in the ascending interferogram and positive in the descending intergerogram, and the eastern lobe is positive in the ascending interferogram but negative in the descending interferogram. In one of the two interferograms, the far-field hanging wall lobe has the same displacement sense as the near-field hanging wall lobe, thus merging into a single lobe, whereas in the other of the two interferograms, the far-field and near-field hanging wall lobes are of the opposite displacement sense, remaining separate. Therefore, one interferogram resembles a two lobed ∞ symbol and the other a three lobed bow-tie, with the condensed, near-field lobe as the central knot.

At more easterly or westerly fault strikes, the InSAR fringe patterns become more complicated. While the condensed, central deformation patterns in the hanging walls directly above the fault planes remain, the broader, far-field lobes characteristic of N–S dip-slip faulting become much less pronounced. This reflects that as fault strike approaches E or W, far-field displacement towards the reverse fault and away from the normal fault is manifest more and more as N–S deformation, to which InSAR is insensitive. One or more smaller lobes appear around either end of the condensed central patch, reflecting localized E–W deformation around the tips of the fault. These produce a complicated four or five lobed deformation pattern, somewhat resembling a balloon animal. A diagnostic characteristic of E- and W-striking dip-slip earthquakes is that the ascending and descending interferograms are mirror images of one another, about an axis perpendicular to the fault center.

Another notable feature of the dip-slip earthquake interferograms is the similarity in fringe patterns between conjugate fault pairs at 90° angles to one another, but striking at similar azimuths. This explains why it is often difficult to differentiate the fault and auxiliary planes in real dip-slip earthquakes. This is especially true when faulting is buried, giving rise to characteristically symmetric "bullseye" fringe patterns (Figure 19, lower right panels) from which it is often not possible to discern fault dip direction (Zhang et al., 2021). Solving this ambiguity may require independent constraints on dip direction, such as from a relocated hypocenter (Karasözen et al., 2018), an alignment of one nodal plane with prominent fault traces (Elliott et al., 2011; Nissen et al., 2022), or triggering relations with other nearby earthquakes (Lohman and Barnhart, 2010).

4.3 Low-angle thrust and normal faulting earthquakes

To simulate InSAR signals for thrust and normal faulting earthquakes on low-angle décollements or detachments, we use a model fault dipping at 10° and buried to 10 km depth. The resulting 3-D deformation is dominated by horizontal displacements at right angles to fault strike; the interferograms will therefore capture this best at northerly or southerly fault strikes. InSAR is also sensitive to smaller amounts of uplift or subsidence, particularly that centered directly above the thrust or normal slip plane.

Figures 8–9 show our model low-angle thrust and normal faulting interferograms, plotted radially by strike. The two sets of interferograms are of the exact opposite displacement sense to one another. Each interferogram contains two or three main lobes arranged above and around the fault. A diagnostic feature at northerly or southerly strikes is that the largest and most prominent deformation lobe appears on the opposite side of the fault in the ascending interferogram to the descending one. As the fault rotates away from N or S, a second deformation lobe on the opposite side of the fault grows in prominence and a third lobe may emerge at one of the two viewing geometries. For E- and W-striking faults, the prominent negative and positive far-field lobes are roughly evenly sized, and in the same arrangement (one on each side of the fault) in the ascending and descending interferograms; although the lobe directly above the fault plane still contains the most fringes. Faint lobes appear to the East (ascending) and West (descending), forming a four-leaf clover pattern. As with the moderate dip-slip earthquakes, when the strike is exactly E or W, the ascending and descending interferograms are mirror images of one another reflected about a N–S axis through the fault center.

4.4 Oblique-slip earthquakes

We model four types of oblique-slip earthquakes, with either left- or right-lateral components, shortening or extensional components, and dipping either steeply at 67.5° (half way between 45° and vertical) or gently at 22.5° (half way between 45° and horizontal). The resulting interferograms (Figures 10–17) thus combine aspects of those presented earlier for strike-slip, moderate dip-slip, and low-angle dip-slip earthquakes.

The interferograms exhibit up to five main deformation lobes, reflecting the complex combinations of vertical and lateral displacements that typify oblique-slip earthquakes (Figures 10–17). However, at certain fault strike and radar illumination angles, simpler butterfly-shaped fringe patterns emerge. For example, steep left-lateral/reverse oblique-slip faults that strike W produce butterfly lobes in the ascending interferogram, while those that strike E produce butterfly lobes in the descending interferogram (Figure 10). These happen to be the fault strike and radar illumination angles at which vertical and E–W deformation components match one another in both location and displacement sense, thus avoiding complicated interference patterns between positive vertical and negative horizontal displacements, and vice versa. However, whereas for ∼E–W vertical strike-slip faults the butterfly patterns are produced simultaneously in the ascending and descending interferograms (Figures 4 and 5), here they are produced in just one of the two. This appears to be a diagnostic characteristic of oblique-slip earthquakes.

4.5 Lookbook summary

Figure 20 summarizes the deformation patterns of our lookbook earthquakes in a single, simplified chart. We can make a few generalizations from this. Strike-slip earthquakes exhibit butterfly shapes when striking E–W, four-leaf clover shapes when striking N–S, and distorted intermediaries at angled orientations. The lobes have the opposite sense of displacement in the ascending and descending interferograms.

Moderate angle dip-slip earthquakes that strike N or S generate a two-lobed ∞ shaped deformation pattern at one viewing angle and a three-lobed bow-tie pattern at the other. There is condensed deformation of consistent displacement sense directly above the fault (in the hanging wall), but the far-field lobes are of the opposite displacement sense in the ascending and descending interferograms. Those that strike E–W are multi-lobed, resembling balloon model animal shapes, and the ascending and descending interferograms are mirror images of one another about an axis perpendicular to the fault center.

Buried, low-angle thrust and normal earthquakes generate simpler patterns in which a single large lobe is characteristic of northerly and southerly strikes (located on the opposite side of the fault in ascending and descending interferograms), and two main lobes are characteristic of westerly and easterly strikes (with mirror imaging as for their moderate angle equivalents).

Lastly, a diagnostic characteristic of oblique-slip earthquakes is the stark difference in lobe patterns between the ascending and descending interferograms, reflecting the complex interplay between vertical and horizontal displacements as resolved by the differing radar illumination angles.

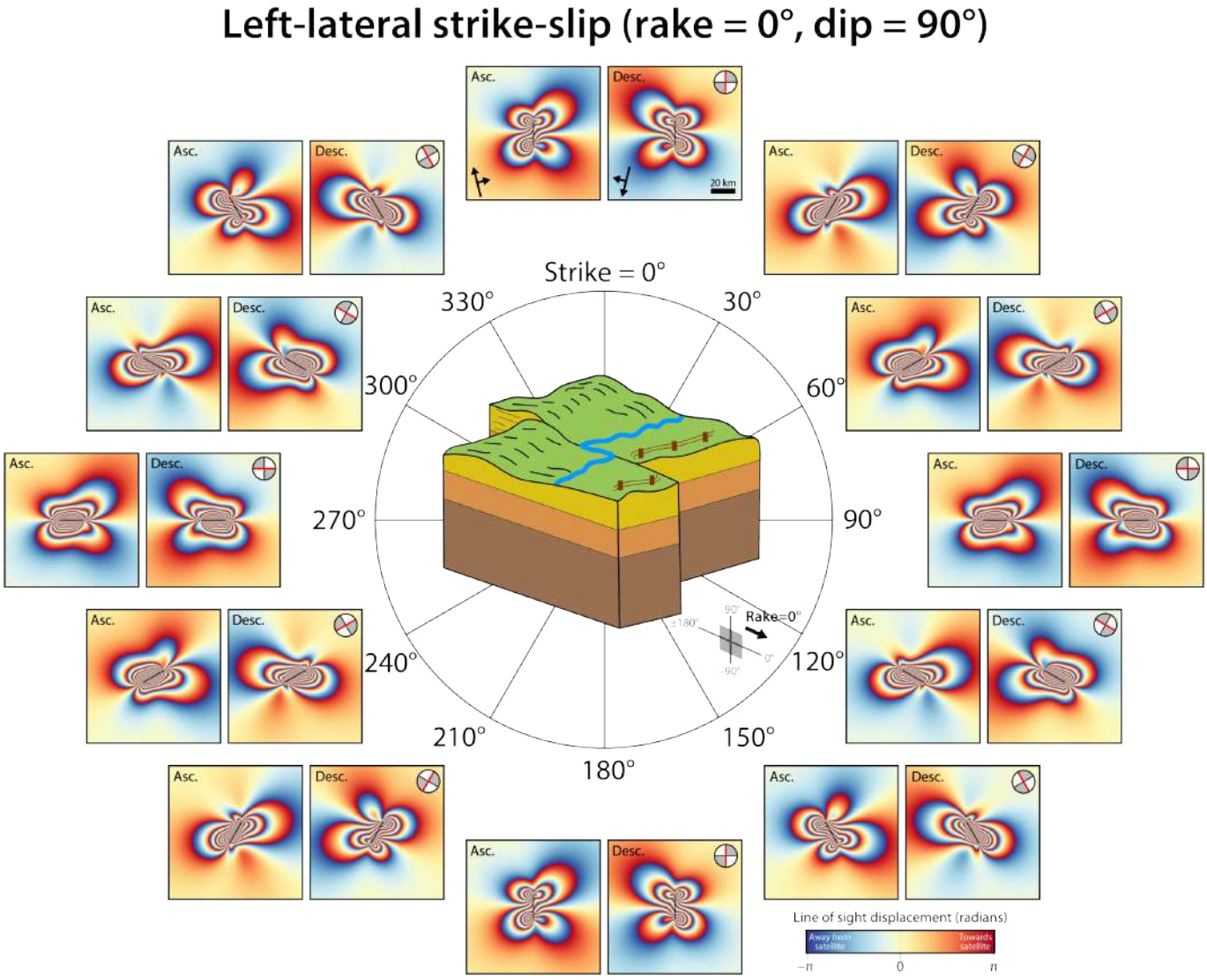

Figure 4 The InSAR lookbook. InSAR forward model wrapped interferograms for variably striking left-lateral strike-slip earthquakes (rake = 0°, dip = 90°). In each figure of the lookbook (Figures 4–17), pairs of (left) ascending and (right) descending interferograms are plotted radially at 30° increments in fault strike around a block diagram illustrating the displayed fault type. In the 0° strike panels, long and short arrows indicate the satellite azimuth and the horizontal component of the LOS vector, respectively (these are the same for all strike values). In all panels, we use the convention that when crossing fringes in the order blue–yellow–red, motion is increasingly towards the satellite, and when crossing fringes in the order red–yellow–blue, motion is increasingly away from the satellite. Solid black lines mark the 20 km-long model fault trace; for gently-dipping faults, a dashed rectangle marks the model fault in plan view. The beach ball in the corner of each descending interferogram is the earthquake focal mechanism, with the fault plane outlined in red.

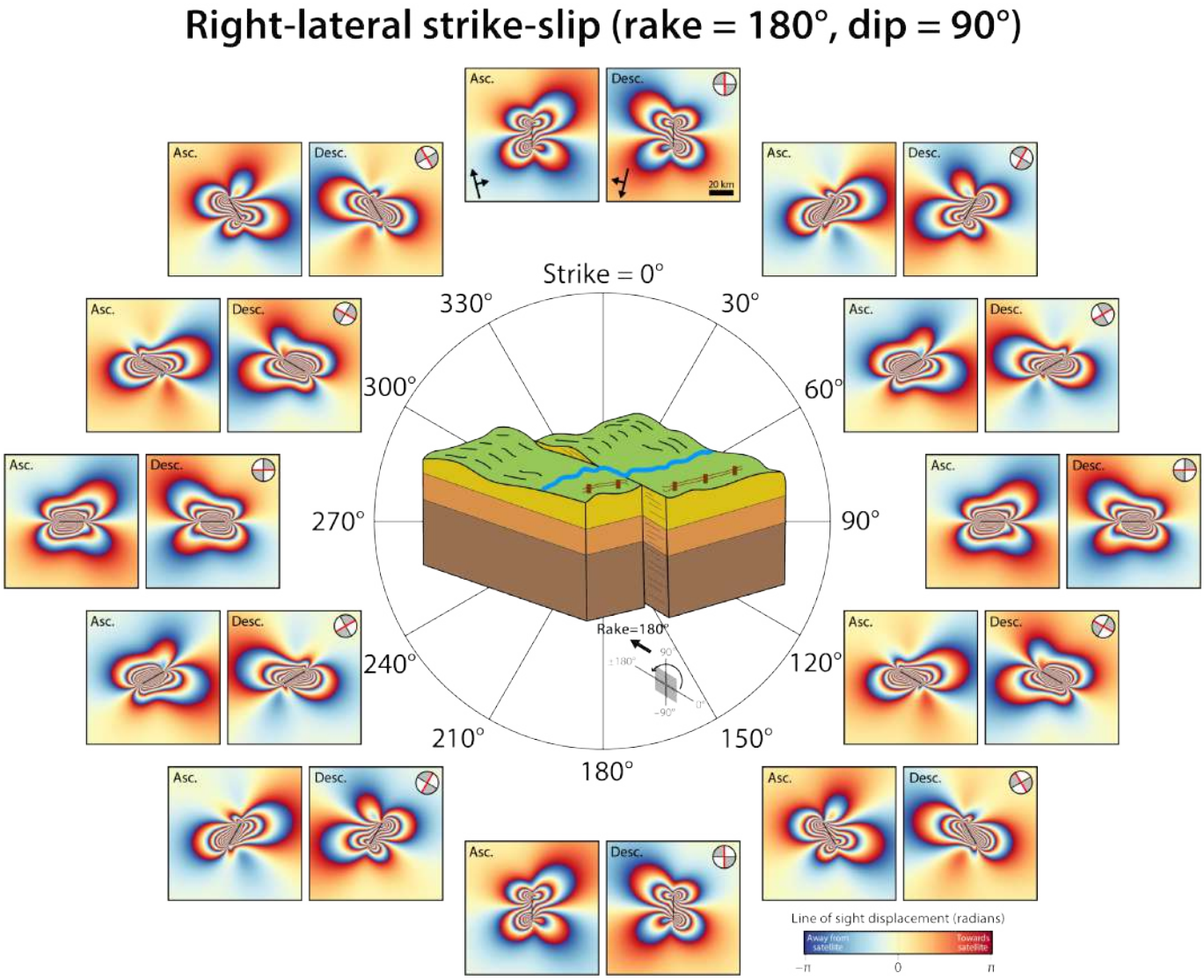

Figure 5 InSAR forward model wrapped interferograms for variably striking right-lateral strike-slip earthquakes (rake = 180°, dip = 90°). Figure details are similar to those in Figure 4.

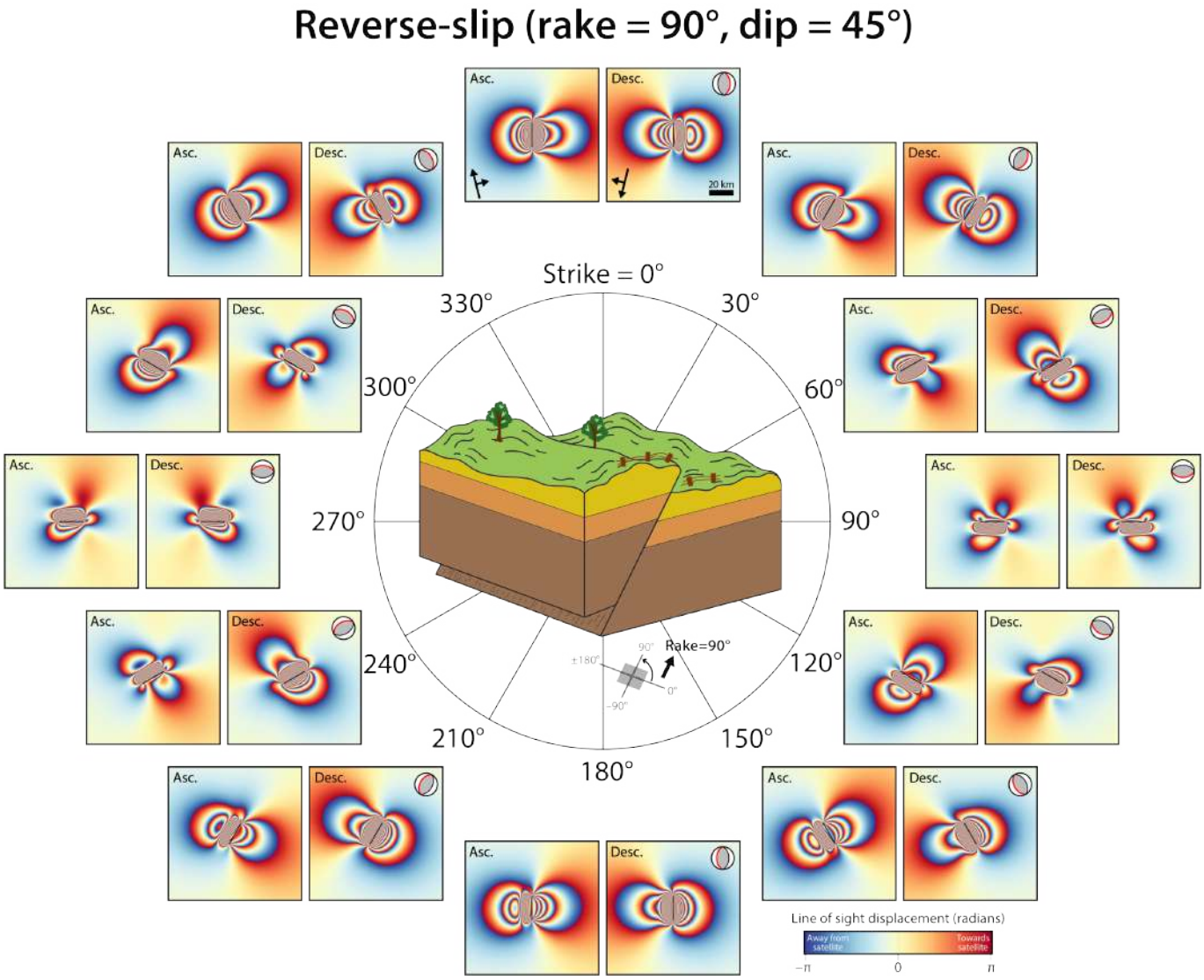

Figure 6 InSAR forward model wrapped interferograms for variably striking reverse faulting earthquakes (rake = 90°, dip = 45°). Figure details are similar to those in Figure 4.

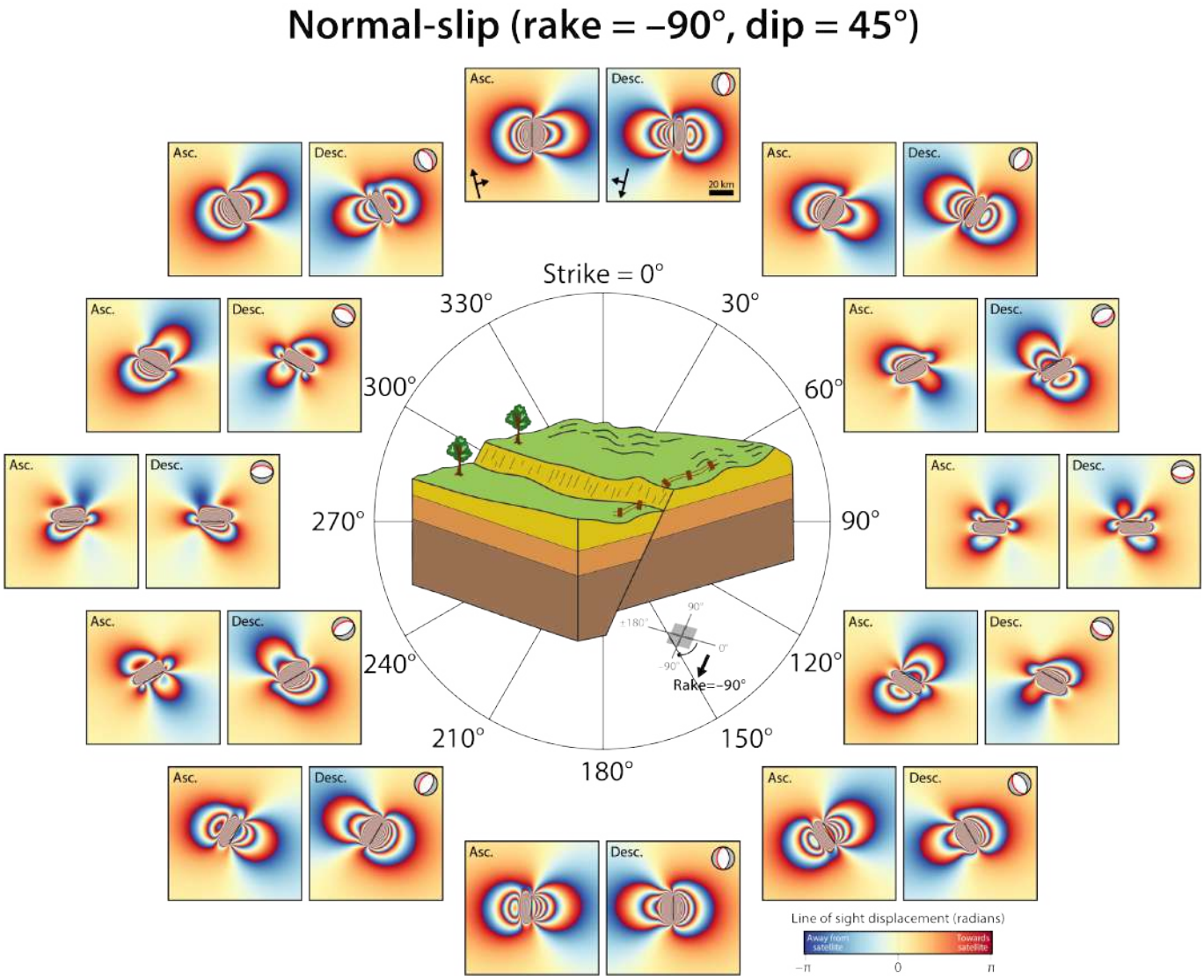

Figure 7 InSAR forward model wrapped interferograms for variably striking normal faulting earthquakes (rake = −90°, dip = 45°). Figure details are similar to those in Figure 4.

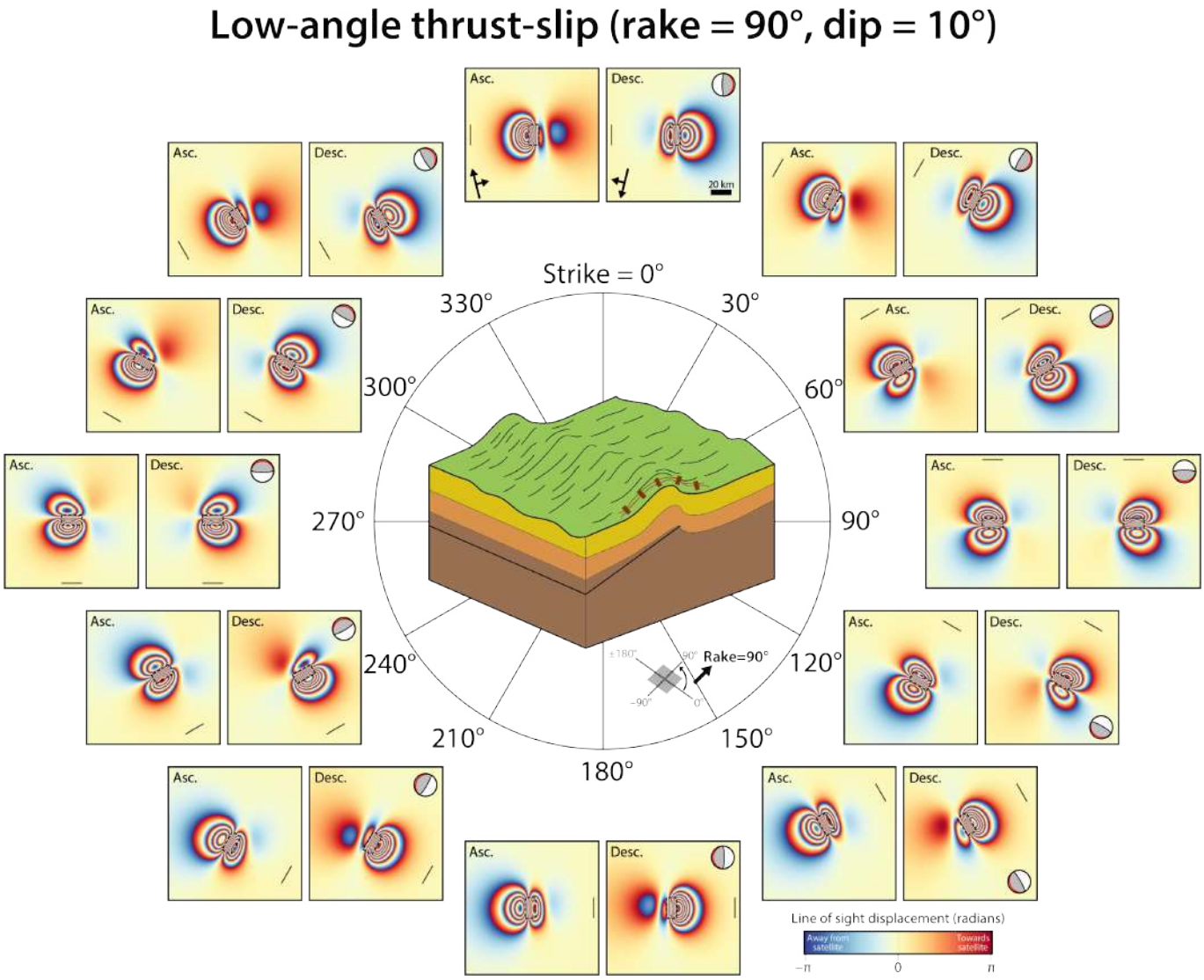

Figure 8 InSAR forward model wrapped interferograms for variably striking, buried, low-angle thrust faulting earthquakes (rake = 90°, dip = 10°). Figure details are similar to those in Figure 4.

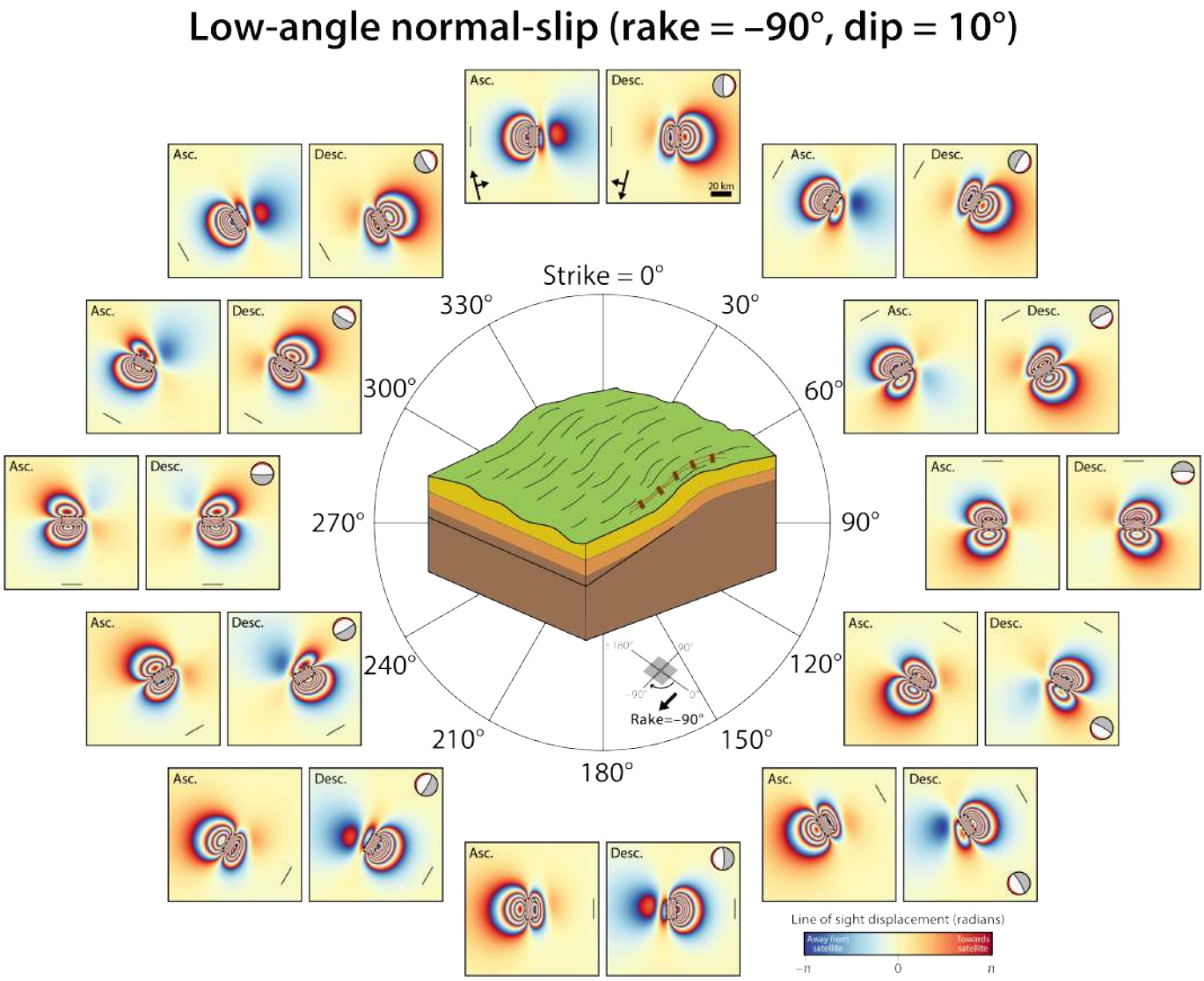

Figure 9 InSAR forward model wrapped interferograms for variably striking, buried, low-angle normal faulting earthquakes (rake = −90°, dip = 10°). Figure details are similar to those in Figure 4.

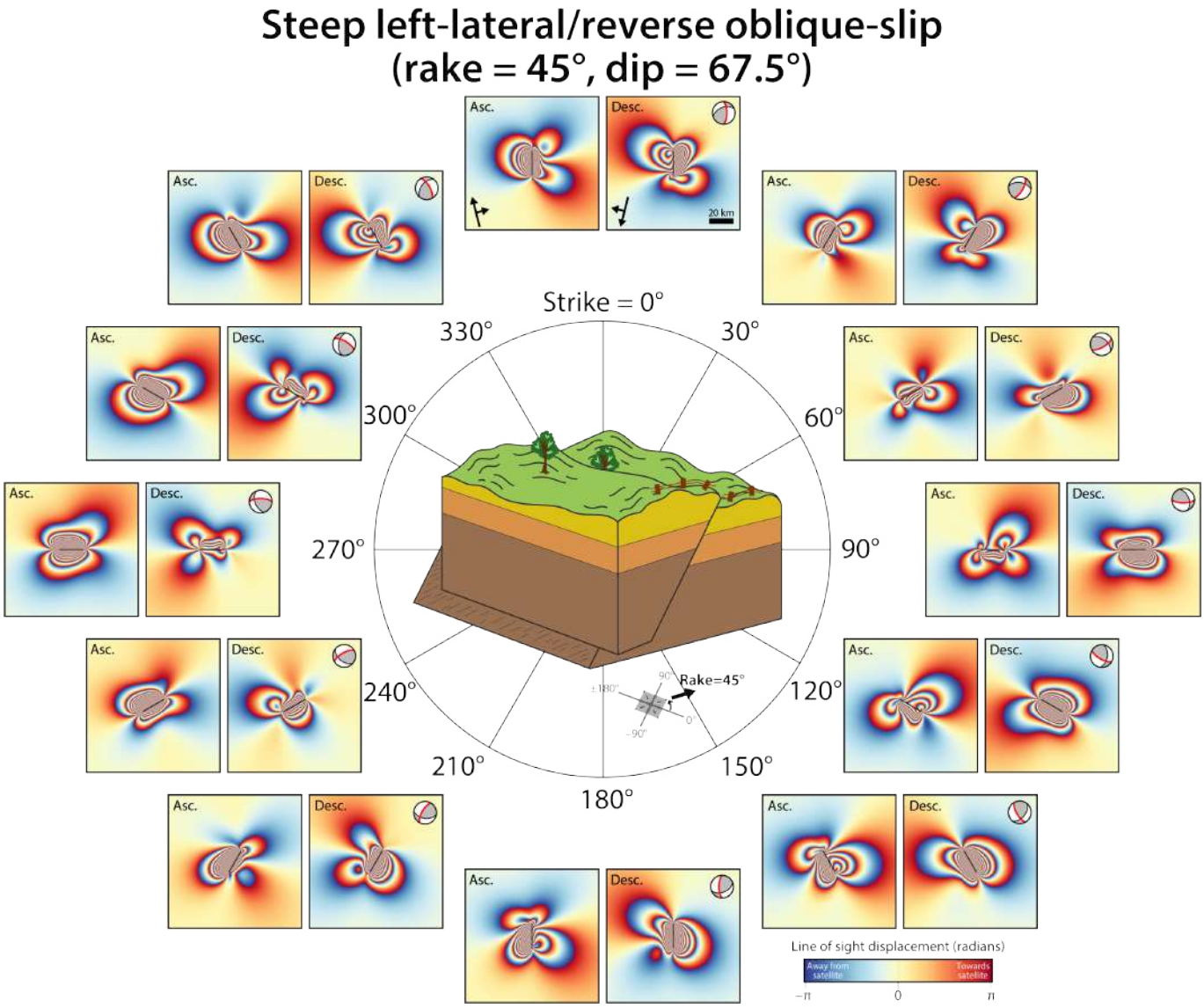

Figure 10 InSAR forward model wrapped interferograms for variably striking, steep-angle, left-lateral/reverse, oblique-slip earthquakes (rake = 45°, dip = 67.5°). Figure details are similar to those in Figure 4.

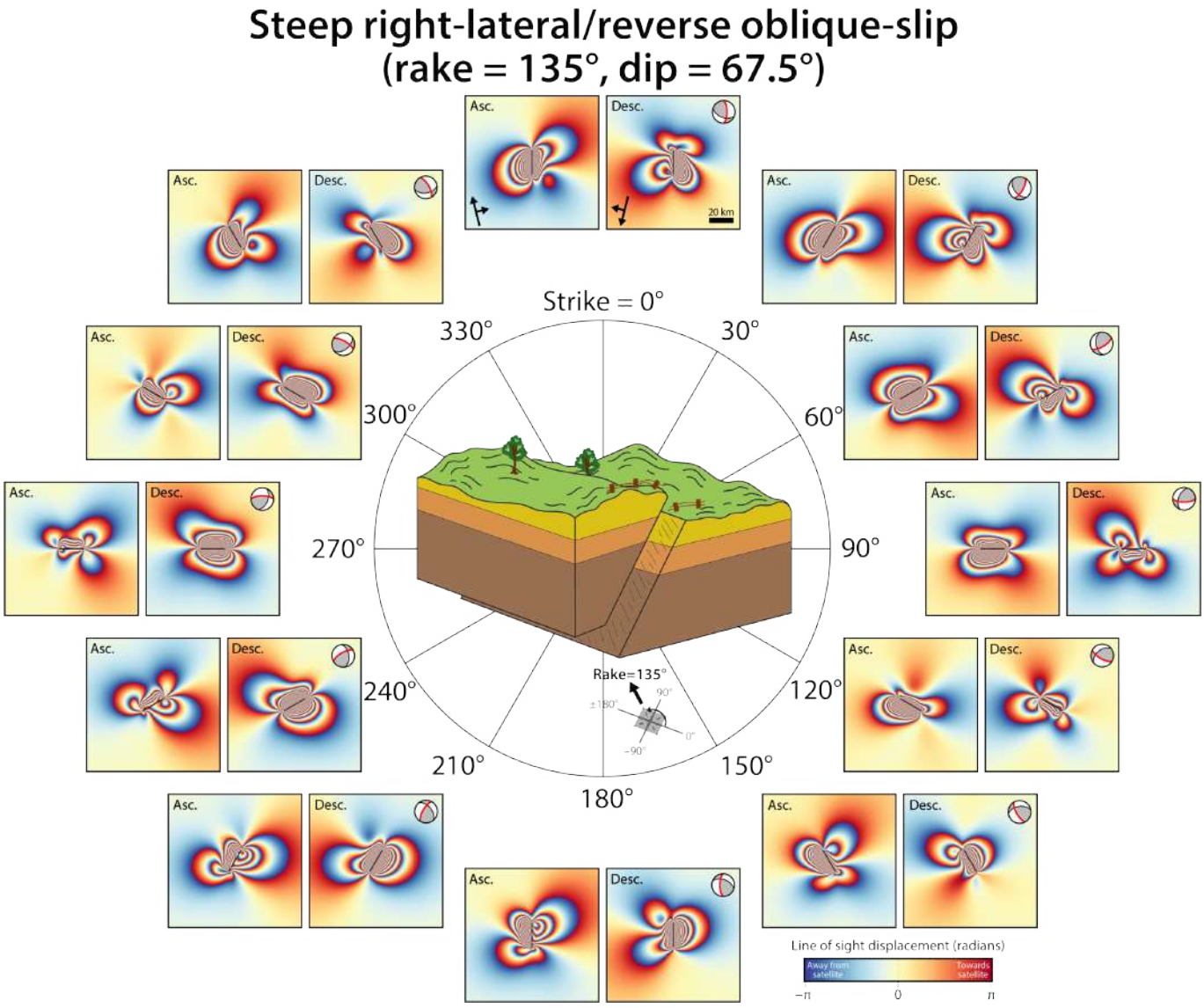

Figure 11 InSAR forward model wrapped interferograms for variably striking, steep-angle, right-lateral/reverse, oblique-slip earthquakes (rake = 135°, dip = 67.5°). Figure details are similar to those in Figure 4.

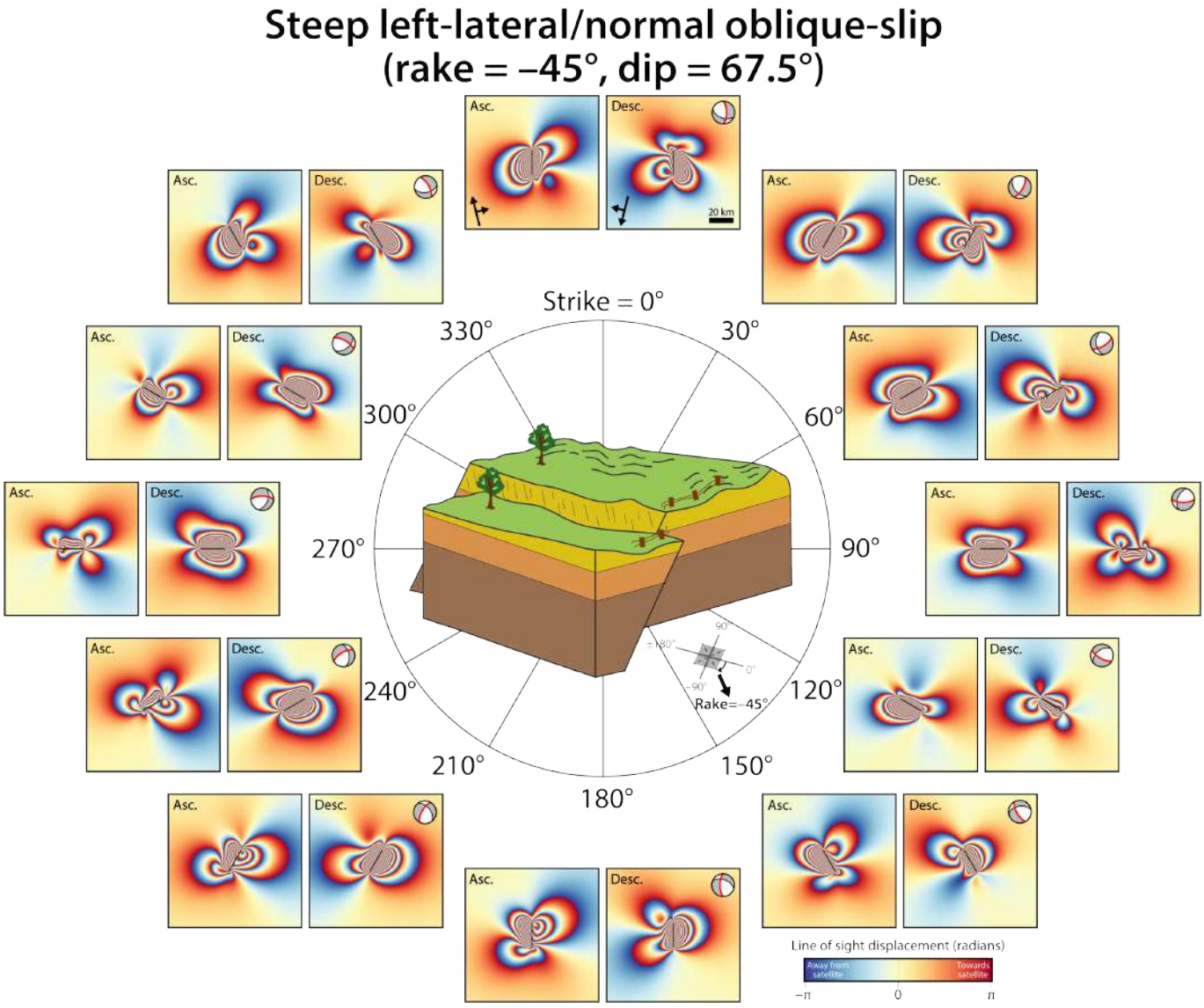

Figure 12 InSAR forward model wrapped interferograms for variably striking, steep-angle, left-lateral/normal, oblique-slip earthquakes (rake = −45°, dip = 67.5°). Figure details are similar to those in Figure 4.

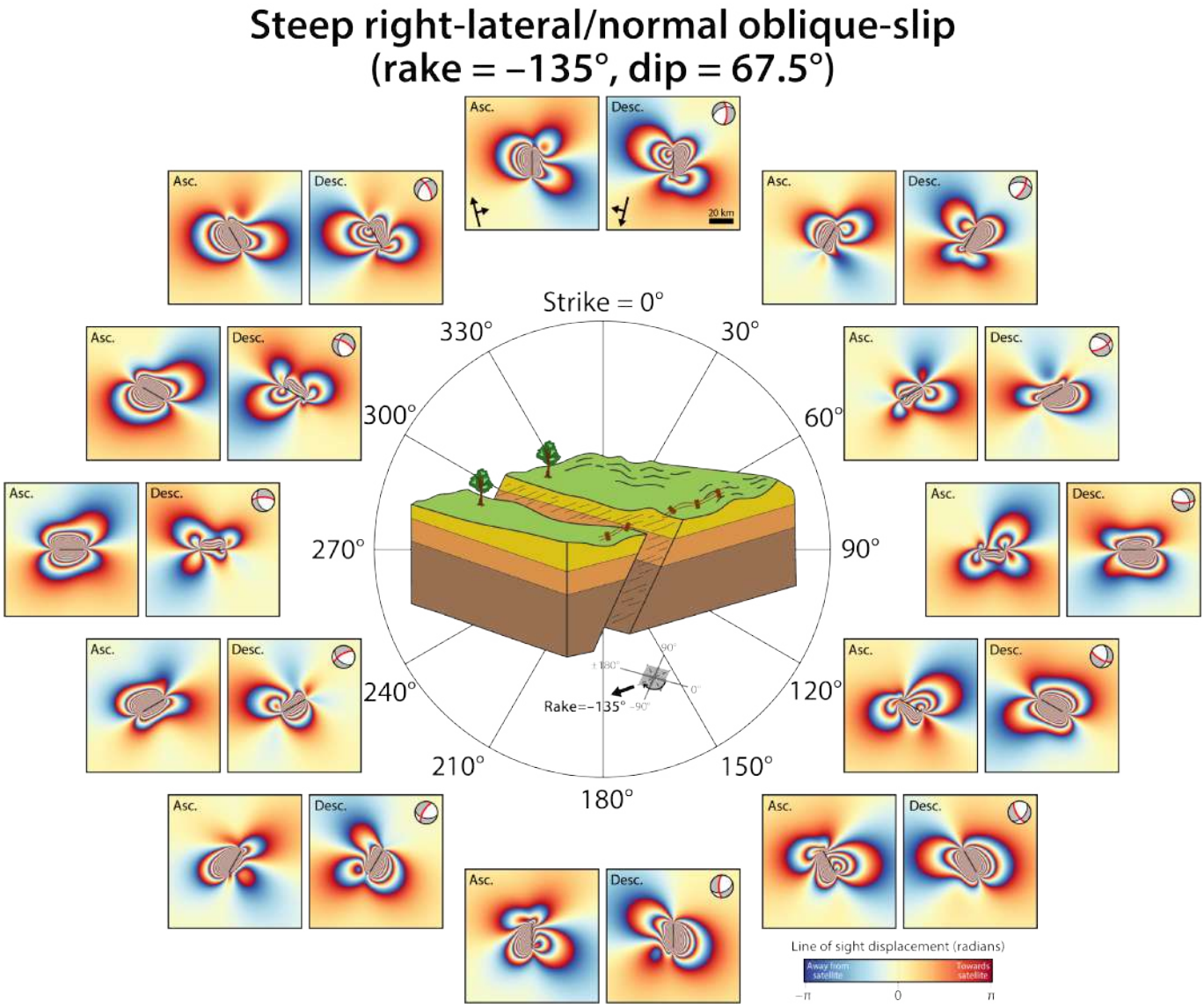

Figure 13 InSAR forward model wrapped interferograms for variably striking, steep-angle, right-lateral/normal, oblique-slip earthquakes (rake = −135°, dip = 67.5°). Figure details are similar to those in Figure 4.

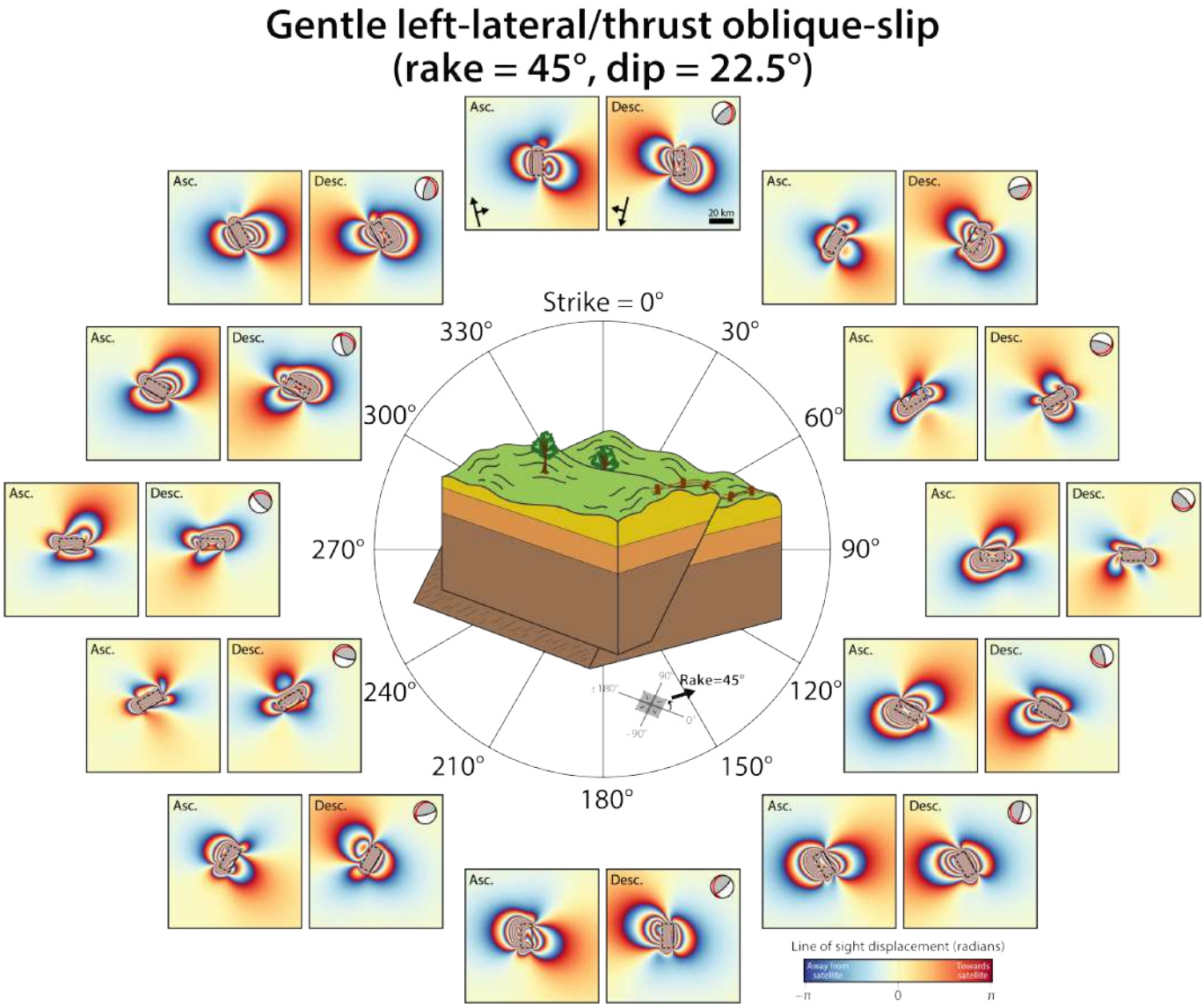

Figure 14 InSAR forward model wrapped interferograms for variably striking, gentle-angle, left-lateral/thrust, oblique-slip earthquakes (rake = 45°, dip = 22.5°). Figure details are similar to those in Figure 4.

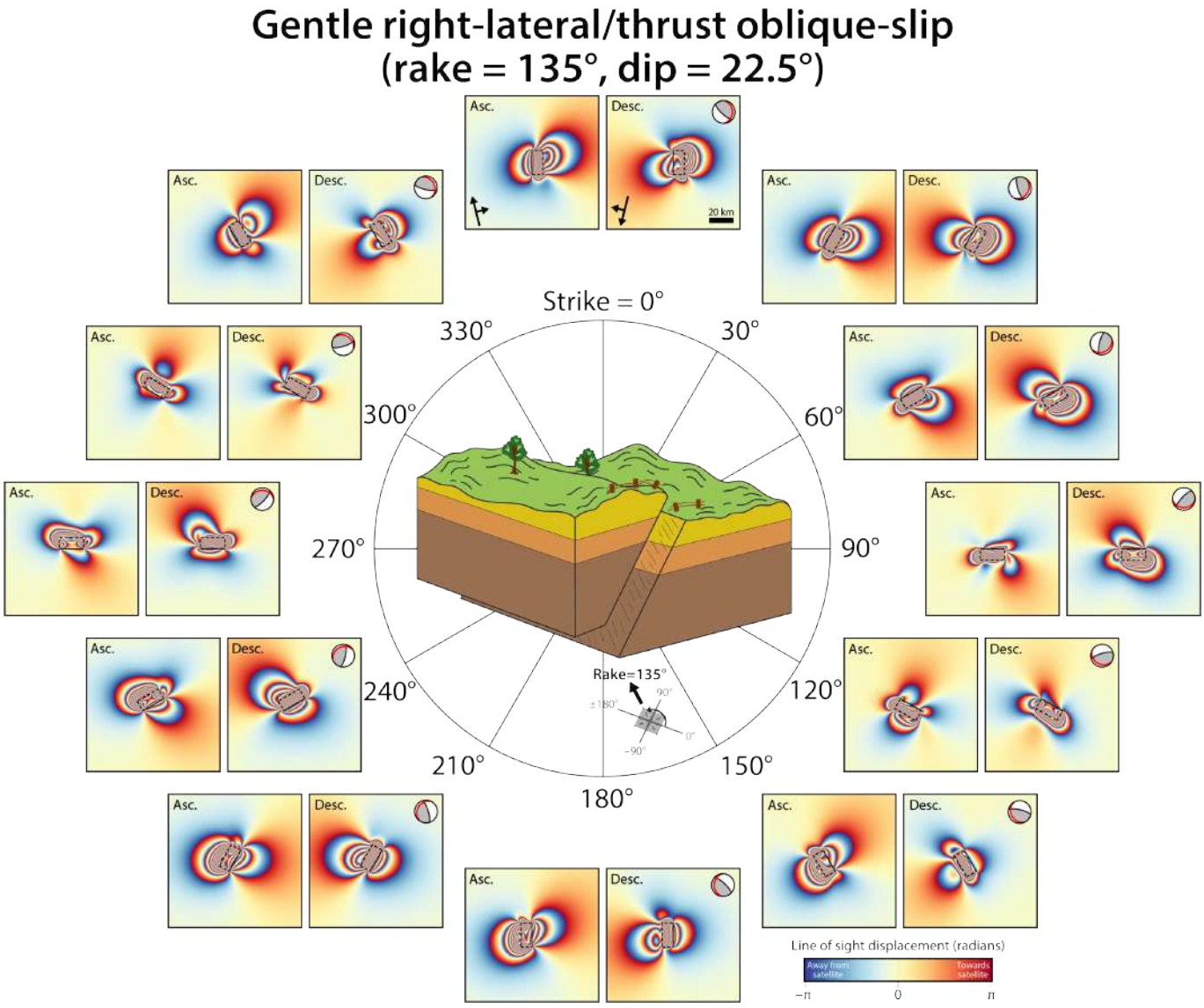

Figure 15 InSAR forward model wrapped interferograms for variably striking, gentle-angle, right-lateral/thrust, oblique-slip earthquakes (rake = 135°, dip = 22.5°). Figure details are similar to those in Figure 4.

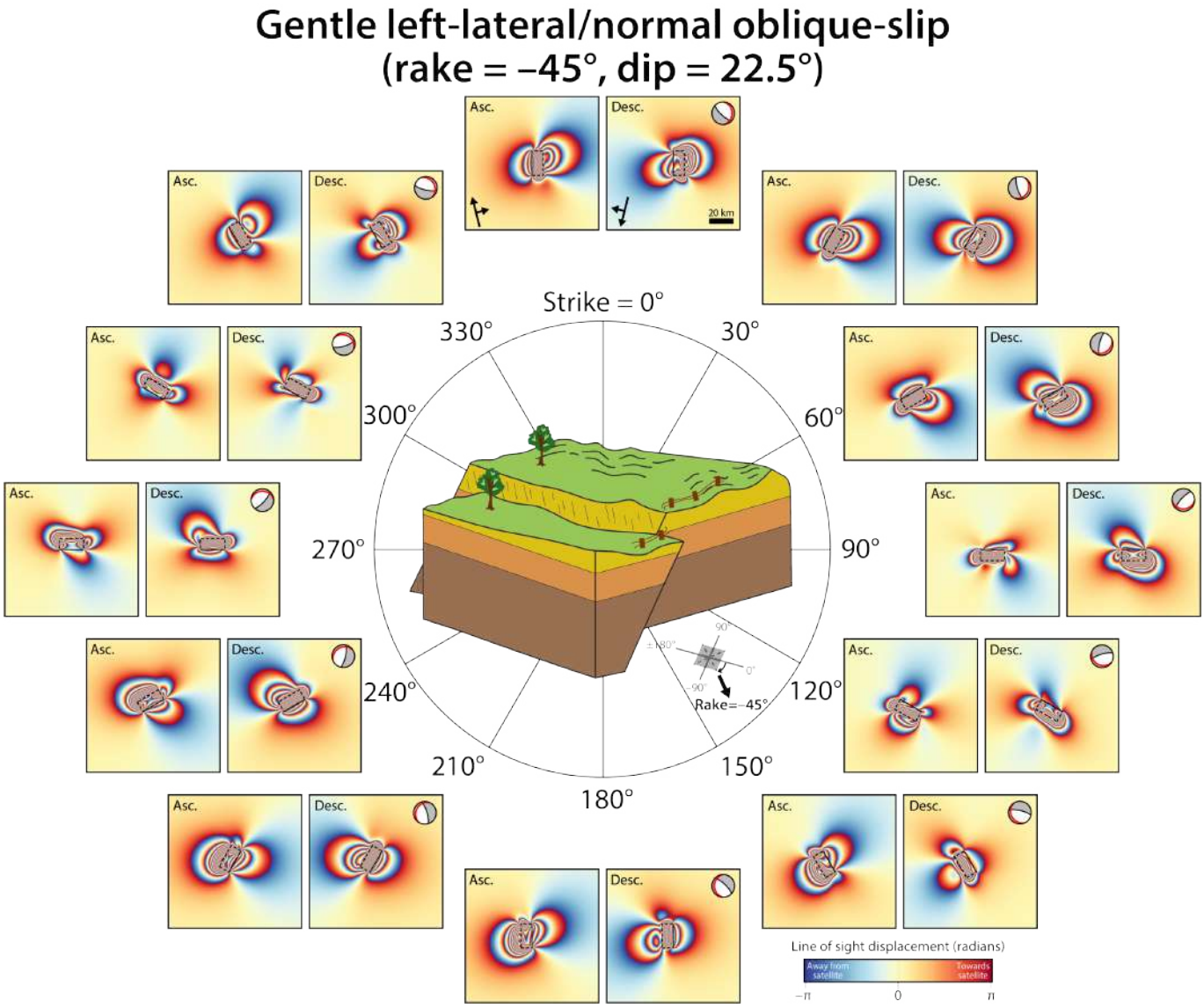

Figure 16 InSAR forward model wrapped interferograms for variably striking, gentle-angle, left-lateral/normal, oblique-slip earthquakes (rake = −45°, dip = 22.5°). Figure details are similar to those in Figure 4.

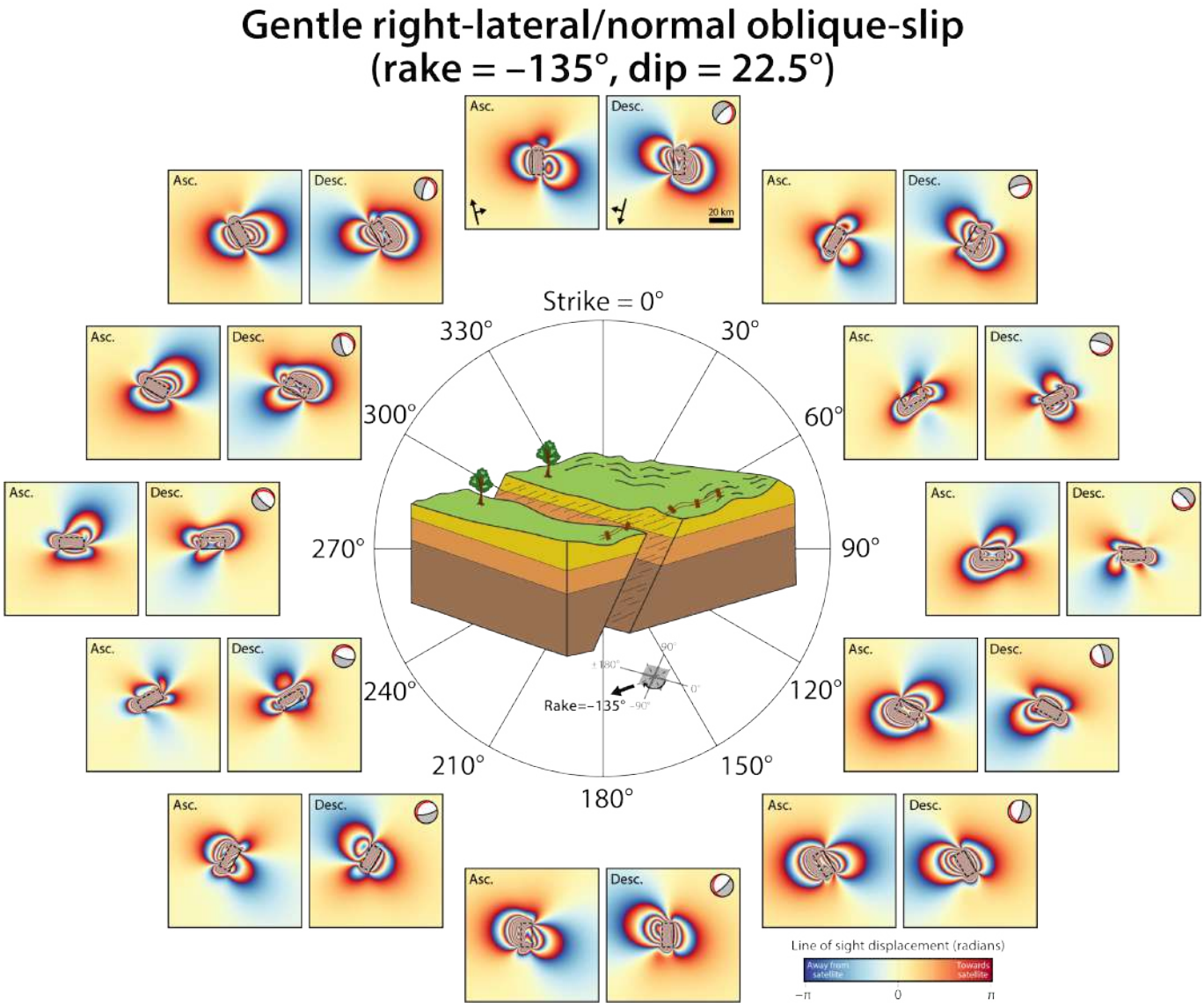

Figure 17 InSAR forward model wrapped interferograms for variably striking, gentle-angle, right-lateral/normal, oblique-slip earthquakes (rake = −135°, dip = 22.5°). Figure details are similar to those in Figure 4.

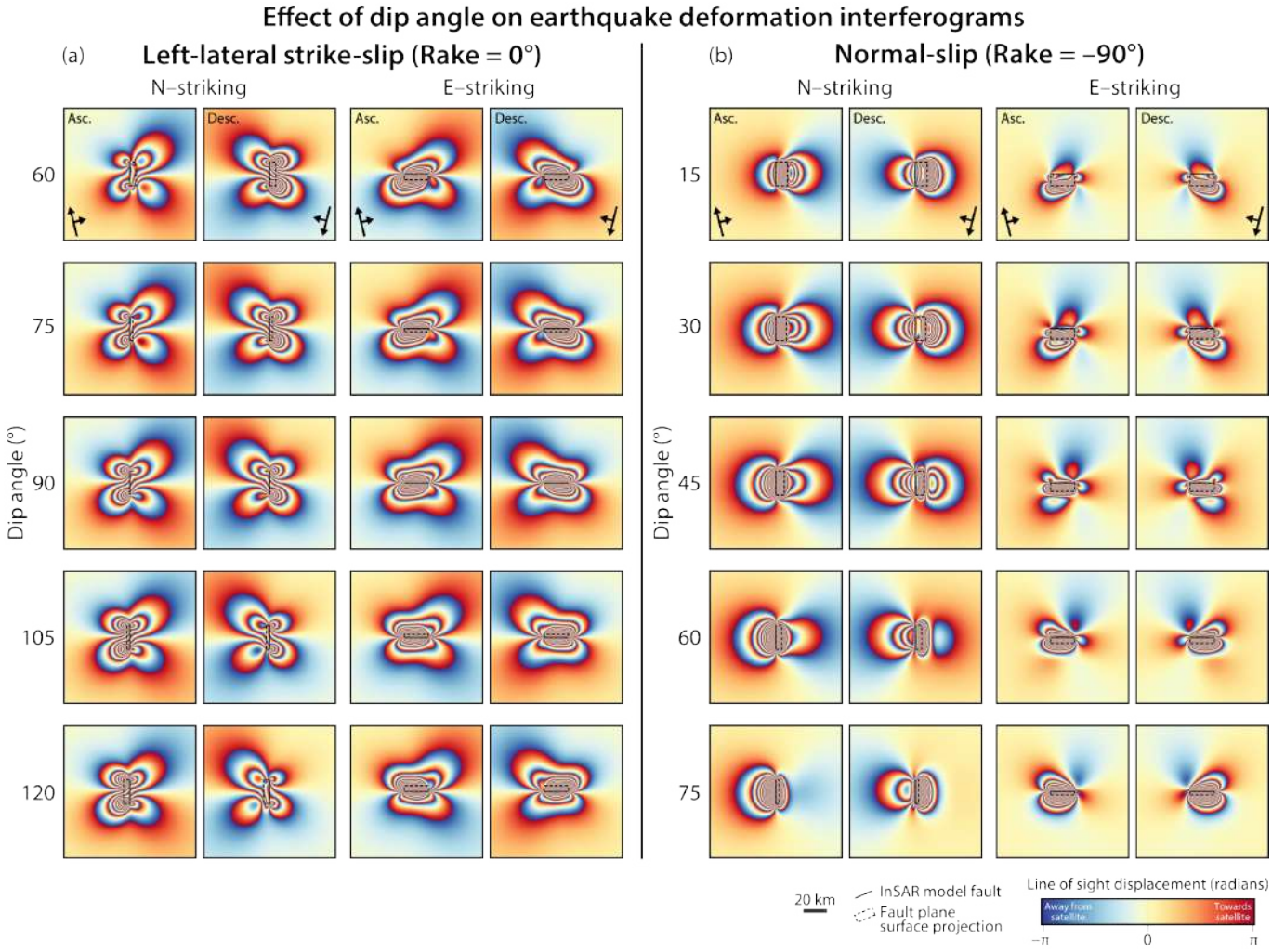

Figure 18 Effect of dip angle on earthquake deformation interferograms for (a) left-lateral strike-slip and (b) normal faulting earthquakes, using the same model set-up as for the main lookbook. For each earthquake type, the first and second columns show ascending (asc.) and descending (desc.) interferogram pairs for N-striking ruptures, the third and fourth columns show equivalent pairs for E-striking ruptures, and the rows show different dip angles. Dips are based on the right hand rule; values of $<90°$ indicate E- or S-dipping faults, while values $>90°$ (i.e. the bottom two rows of strike-slip earthquakes) indicate W- and N-dipping faults. Solid black lines mark the 20 km-long model fault trace, and a dashed rectangle marks the model fault in plan view.

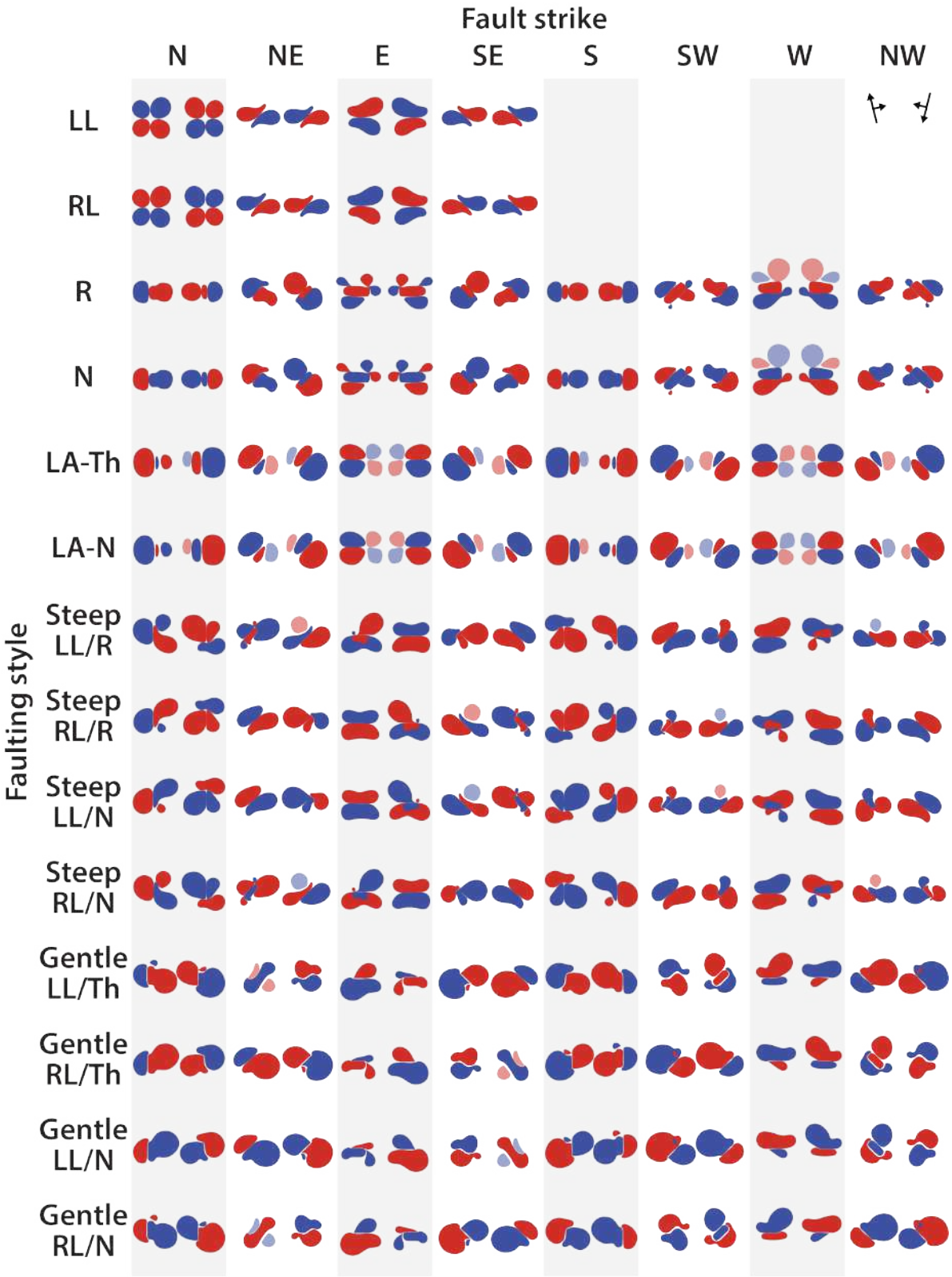

Figure 20 A chart summarizing InSAR deformation lobe patterns by earthquake fault type and orientation. Rows represent the fourteen earthquake fault types (LL = left-lateral, RL = right-lateral, R = reverse, N = normal, LA = low angle, Th = thrust) and columns show eight strikes at 45° increments from North. For each combination of earthquake type and strike, we plot simplified ascending track (left) and descending track (right) lobe patterns, with red and blue indicating motion towards or away from the satellite, respectively. Faded colors are used where lobes are prominent in our wrapped interferograms, but contain less than a full fringe cycle. Because our model strike-slip earthquakes are on vertical faults, deformation at strikes of S, SW, W and NW mimics that at strikes of N, NE, E and SE, respectively. Long and short arrows in the top right of the figure indicate the satellite azimuth and the horizontal component of the LOS vector, respectively, for ascending track (left) and descending track (right) interferograms.

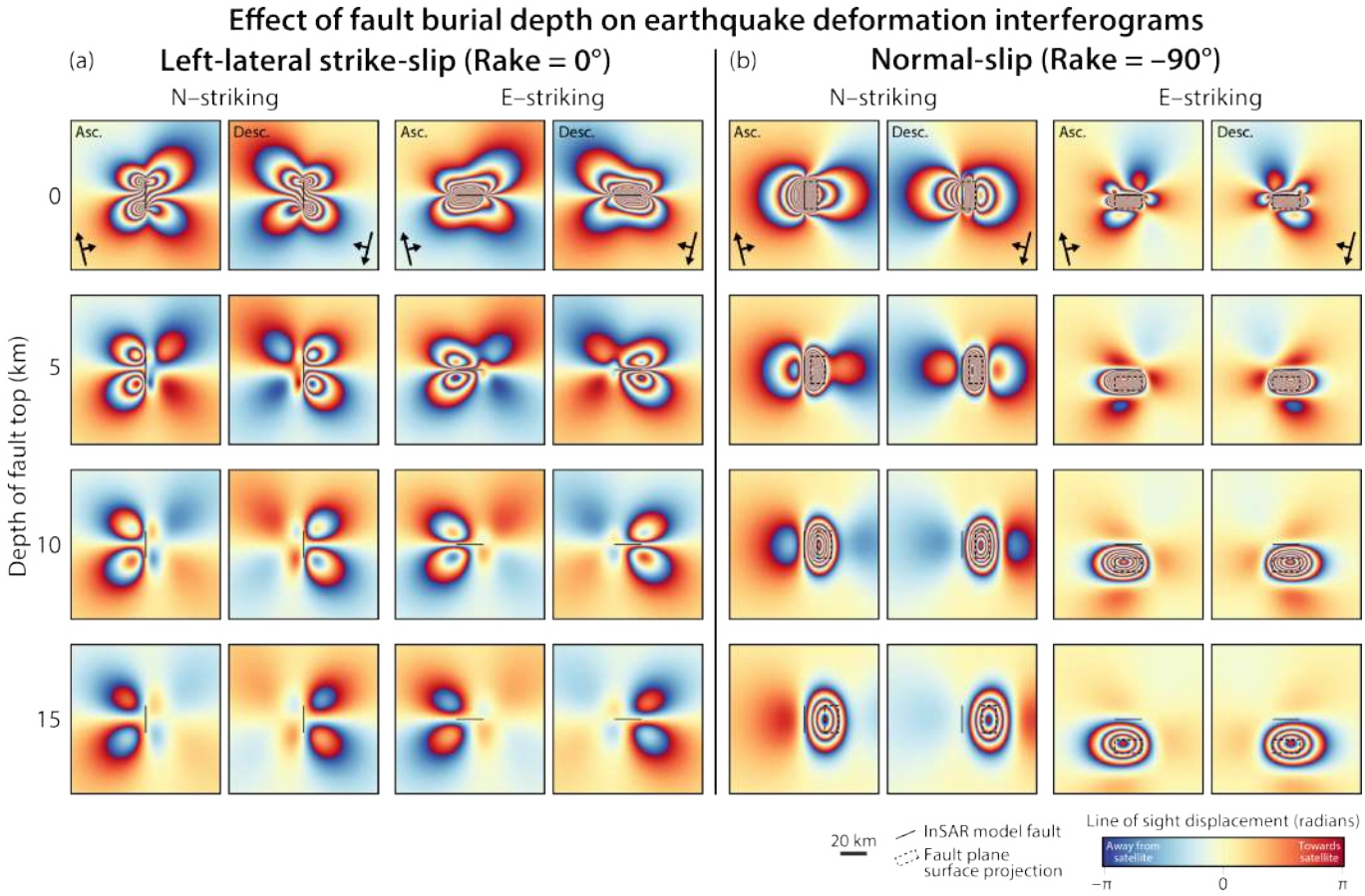

Figure 19 Effect of fault burial depth on earthquake deformation interferograms for (a) vertical left-lateral strike-slip and (b) 45°-dipping normal faulting earthquakes, using the same model set-up as for the main lookbook. For each earthquake type, the first and second columns show ascending (asc.) and descending (desc.) interferogram pairs for N-striking ruptures, the third and fourth columns show equivalent pairs for E-striking ruptures, and the rows show different burial depths of the fault top. Solid black lines mark the 20 km-long model fault trace, and for the normal faults, a dashed rectangle marks the model fault in plan view.

5 Real earthquake comparisons

To demonstrate the application of our InSAR lookbook, we now compare our model interferograms with those of sixteen, real-world earthquakes (Table 2). These were selected firstly because they all display clear InSAR fringe patterns for comparison with our synthetic interferograms, and secondly because they span a wide range of mechanisms and orientations. Some of the events have published InSAR fault slip models, which we discuss later in this section. Most of the interferograms were obtained from the COMET LiCSAR portal (Lazecký et al., 2020; Watson et al., 2023), which provides Sentinel-1 interferograms of large earthquakes since 2019 (see Data and code availability). For two of the earthquakes, interferograms were obtained directly from the authors of published studies (Funning et al., 2005; Kim and Han, 2023). We scaled the real earthquake interferograms to match our lookbook model interferograms in size on the page, and applied the same LOS displacement convention (see Section 3.1). Therefore, the real earthquake deformation lobes may differ from the lookbook comparison models in both size and amplitude, according to the earthquake magnitude and depth. However, as described in Section 3.3, the purpose is to compare the general lobe patterns taking into account their LOS displacement sense.

5.1 Strike-slip examples

The 2003 $\mathrm{M_w}$ 6.6 Bam, Iran earthquake generated the four-leaf clover deformation pattern characteristic of N–S right-lateral strike-slip faulting (Figure 21a). Though the earthquake occurred in a region of previously sparse seismicity, it was also directly along strike from the major, N–S Gowk right-lateral fault system (Walker and Jackson, 2002), so the fault style and orientation were not surprising. The interferograms also display a narrow, N–S trend of decorrelation which marks a surface rupture (Funning et al., 2005). A dense fringe lobe on the east side of the surface rupture and in between the larger deformation lobes, a feature not evident in our simpler model, partly reflects right-lateral/reverse oblique slip on a shallow splay off the main right-lateral fault (Funning et al., 2005).

The 2022 $\mathrm{M_w}$ 6.7 Menyuan, China earthquake in the Qilian Shan mountains is characterized by butterfly-shaped deformation lobes that are symmetric in the descending interferogram but skewed in the ascending one, closely mimicking our lookbook interferograms for WNW–ESE, left-lateral strike-slip earthquakes (Figure 21b). The earthquake epicenter lies on the well known, ESE-trending, left-lateral Haiyuan fault (Li et al., 2023), so the relevant lookbook model would have been easily anticipated. The pattern arises because the Haiyuan fault is exactly perpendicular to the descending look vector but slightly oblique to the ascending one.

The 2020 $\mathrm{M_w}$ 6.4 Petrinja, Croatia earthquake differs from the earlier examples in that it was the first event of $\mathrm{M_w} \geq 6.0$ in its region since modern records began (U.S. Geological Survey, 2017, Advanced National Seismic System Comprehensive Earthquake Catalogue, USGS ANSS ComCat). An elongate zone of decorrelation masks details of the near-field deformation but hints at an approximately NW–SE-trending rupture (Figure 21c). Without an expectation for the fault kinematics, lookbook users could instead utilize our fixed strike models for 150°- or 330°-striking faults (Figures S2f and S2l) to find the closest rupture mechanism. The observed pattern duly matches that for a rake of 180°, indicating a right-lateral strike-slip earthquake, consistent with both rapid moment tensor solutions and subsequently published InSAR slip models (Xiong et al., 2021).

The 2023 $\mathrm{M_w}$ 6.9 Murghob, Tajikistan earthquake in the Pamir mountains exhibits a skewed butterfly fringe pattern in the ascending interferogram and a four-leaf clover in the descending one, closely resembling our model interferograms for a NNE–SSW left-lateral earthquake (Figures 21d). The NNE trend is hinted at in a zone of decorrelation, though coherence is rather poor across the entire interferogram, likely owing to steep topography and/or snow cover. Published InSAR slip models confirm our inference of NNE-trending left-lateral faulting (Liu et al., 2024; Shi et al., 2023).

5.2 Dip-slip examples

The 2020 $\mathrm{M_w}$ 6.3 Hotan, China earthquake occurred in the northwestern Tibetan plateau, a region of widespread ∼E–W-directed extension (e.g., Fang et al., 2024). There is some disagreement on its source mechanism, with the USGS W-phase model suggesting pure normal slip on a NNE- or SSW-striking plane, and the Global Centroid Moment Tensor (GCMT) catalog indicating oblique slip on a N-striking right-lateral/normal fault or a SW-striking left-lateral/normal fault. This is a good test of whether the lookbook can resolve such an ambiguity. We find that the closest lookbook solutions to the USGS and GCMT nodal planes (Figures 7, 12, 13) are a poor match to the observed InSAR deformation (Figure 22a). Instead, our lookbook interferograms for a S-striking normal fault seem to match the data best. This is borne out by published InSAR slip models with strike 186°, a few degrees off our lookbook value (Zhu et al., 2021; Yu et al., 2021). However, N-striking normal faulting will produce a rather similar fringe pattern and, with the condensed central lobe and parts of the western far-field lobe significantly decorrelated, we consider the fault and auxiliary planes to be ambiguous in this case.

The 2020 $\mathrm{M_w}$ 6.3 Nima, China earthquake in the central Tibetan plateau illustrates a similar deformation pattern, with a dense, near-field fringe ellipse in both interferograms, and two (ascending) or three (descending) deformation lobes in total (Figure 22b). Our NNE-striking normal fault model (strike, dip, and rake of 30°, 45°, and −90°) reproduces the data best, but a SSW-striking normal fault is also a reasonably close match. The preferred mechanism compares well with a published InSAR inversion that yields strike, dip and rake of 28°, 48°, and −87° (Li et al., 2021a). Other source inversions involve additional geometric complexities beyond the scope of our lookbook. For example, Liu et al. (2023) propose a three-segmented fault model and Gao

Table 2 Real earthquakes used as lookbook comparisons. Dates of earthquakes and ascending and descending InSAR acquisitions are listed as dd.mm.yr in Coordinated Universal Time (UTC). Fault refers to our interpretation from the lookbook, given as strike followed by kinematics (LL = left-lateral, RL = right-lateral); question marks indicate where the conjugate nodal plane could equally be the fault. We know of no examples of InSAR observations of earthquakes on low-angle normal faults. Unless noted otherwise by asterisks, interferograms were obtained from the COMET LiCSAR Sentinel-1 database (see Data and code availability).

Earthquake	Date	M_w	Fault	Ascending	Descending
Strike-slip (Figure 21)					
Bam, Iran	26.12.03	6.6	N, RL	16.11.03–25.01.04*	03.12.03–11.02.04*
Menyuan, China	07.01.22	6.7	ESE, LL	05.01.22–17.01.22	29.12.21–10.01.22
Petrinja, Croatia	29.12.20	6.4	NW, RL	18.12.20–30.12.20	17.12.20–04.01.21
Murghob, Tajikistan	23.02.23	6.9	NNE?, LL	03.02.23–23.03.23	21.02.23–05.03.23
Dip-slip (Figure 22)					
Hotan, China	25.06.20	6.3	S?, Normal	22.06.20–04.07.20	17.06.20–29.06.20
Nima, China	22.07.20	6.3	NNE?, Normal	18.07.20–30.07.20	02.07.20–26.07.20
Thessaly, Greece	03.03.21	6.3, 6.0†	NW, Normal	25.02.21–09.03.21	03.03.21–09.03.21
Herāt, Afghanistan	07.10.23	6.3, 6.3	W, Reverse	25.09.23–07.10.23	26.09.23–08.10.23
Low-angle thrust (Figure 23)					
Jiashi, China	19.01.20	6.0	W, Thrust	16.01.20–28.01.20	10.01.20–22.01.20
Hormozgan, Iran	14.11.21	6.0, 6.4	E, Thrust	13.11.21–25.11.21	09.11.21–03.12.21
Ganaveh, Iran	18.04.21	5.8	NW, Thrust	02.04.21–20.05.21	10.04.21–22.04.21
Marrakesh-Safi, Morocco	08.09.23	6.8	ENE?, Thrust	03.09.23–15.09.23	04.09.23–16.09.23
Oblique slip (Figure 24)					
Mindanao, Philippines	15.12.19	6.8	NW, LL/Reverse	13.12.19–25.12.19	13.12.19–19.12.19
Khövsgöl, Mongolia	11.01.21	6.7	NNW, RL/Normal	21.06.20–20.06.21**	07.01.21–19.01.21
Wushi, China	22.01.24	7.0	WSW, LL/Reverse	14.01.24–26.01.24	13.01.24–25.01.24
Monte Cristo Range, USA	15.05.20	6.5	ENE, LL/Normal	11.05.20–29.05.20	11.05.20–29.05.20

*Both Envisat interferograms (half-wavelength of 2.77 cm) are from Funning et al. (2005).
**The ALOS-2 ascending interferogram (half-wavelength of ∼12 cm) is from Kim and Han (2023).
†The second earthquake occurred on 04.03.21.

et al. (2022) suggest an S-shape geometry with varying strike and dip angles.

The 2021 M_w 6.3 and 6.0 Thessaly, Greece earthquake doublet exhibits a more convoluted fringe pattern than the Tibetan normal faulting events described above, owing in part to the fact that its fault strike is deviating away from N–S (Figure 22c). Both interferograms contain a condensed, NW-trending fringe ellipse moving away from the satellite, surrounded by two (ascending) or 3–4 (descending) smaller deformation lobes. The signal compares quite well to our lookbook interferograms for a WNW-striking normal faulting earthquake, though the far-field lobes appear somewhat distorted. This, and the elongated condensed fringes, likely owe to the involvement of two along-strike segments separated by a fault bend and stepover, as revealed by published InSAR models (Yang et al., 2022).

The October 7 2023 Herāt doublet in the Paropamisus mountains of NW Afghanistan involved a pair of M_w 6.3 earthquakes ∼30 minutes apart, and was followed by two more M_w 6.3 events on October 11 and 15 which are not captured in the interferograms presented here. Moment tensors for the October 7 earthquakes from the USGS, GCMT, and waveform modelling by Zhao et al. (2025) support moderate angle N- or S-dipping reverse faulting. Both interferograms contain an elongate (E–W) lobe of deformation towards the satellites in the north, and a broad but subtle lobe of deformation away from the satellites in the south, more consistent with N-dipping reverse faulting (Figures 22d), a geometry confirmed by inverse modelling (Zhao et al., 2025). Upon closer inspection, the ascending and descending interferograms also exhibit small "tear-drop" lobes at the eastern and western fault tips, respectively, a pattern that closely matches our lookbook summary model in Figure 20.

5.3 Low-angle thrust examples

The 2020 M_w 6.0 Jiashi, China earthquake in the southwestern Tian Shan exhibits a pair of elongate, E–W-trending deformation lobes in both ascending and descending interferograms. The northern lobes contain displacements away from the satellite and the southern lobes contain about double those displacements towards the satellite (Figure 23a). This pattern is characteristic of a W-striking (N-dipping) low-angle thrust fault centered between the two lobes and projecting to the surface some distance to the South. The elongate fringe pattern reflects that the real earthquake involved a much greater length-to-width ratio than our model value of 2, as confirmed by inverse modelling and aftershock relocations (Wang et al., 2022).

The 2021 Hormozgan, Iran doublet in the frontal Zagros mountains involved M_w 6.0 and 6.4 earthquakes about 90 seconds apart, which cannot be separated by

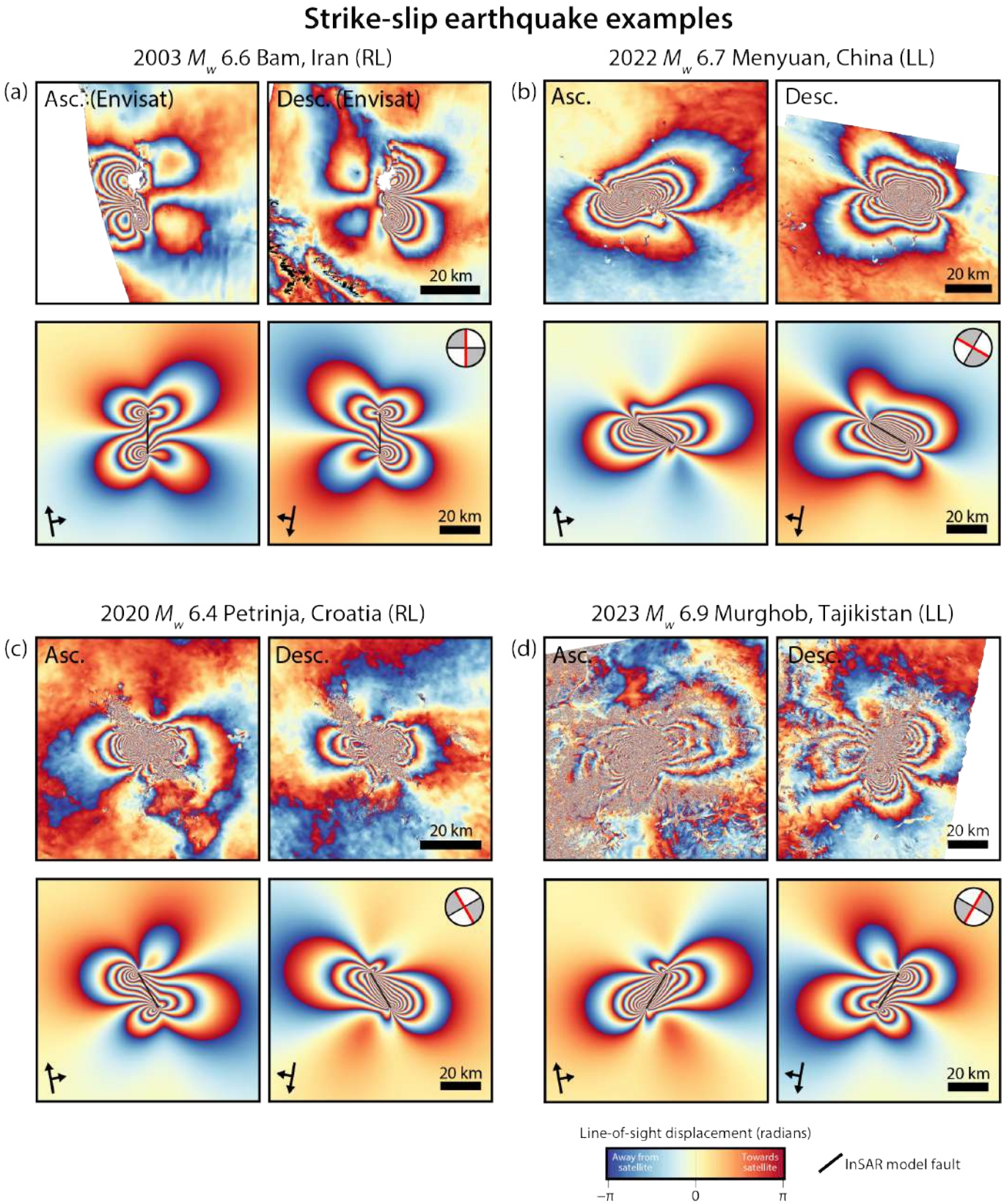

Figure 21 Comparisons between real strike-slip earthquake deformation interferograms (top rows) and our closest-matching lookbook models (bottom rows) for the (a) 2003 $\mathrm{M_w}$ 6.6 Bam, Iran, (b) 2022 $\mathrm{M_w}$ 6.7 Menyuan, China, (c) 2020 $\mathrm{M_w}$ 6.4 Petrinja, Croatia, and (d) 2023 $\mathrm{M_w}$ 6.9 Murghob, Tajikistan earthquakes (see Table 2 for earthquake details). Left and right columns are ascending and descending interferograms, respectively. For the Bam earthquake, the Envisat interferograms half-wavelength is 2.77 cm (panel a, top row) similar to our models. Thick black lines indicate our model faults and conjugate arrows denote the satellite azimuth and line-of-sight. The beach ball is the earthquake focal mechanism of our InSAR model, with the fault plane outlined in red.

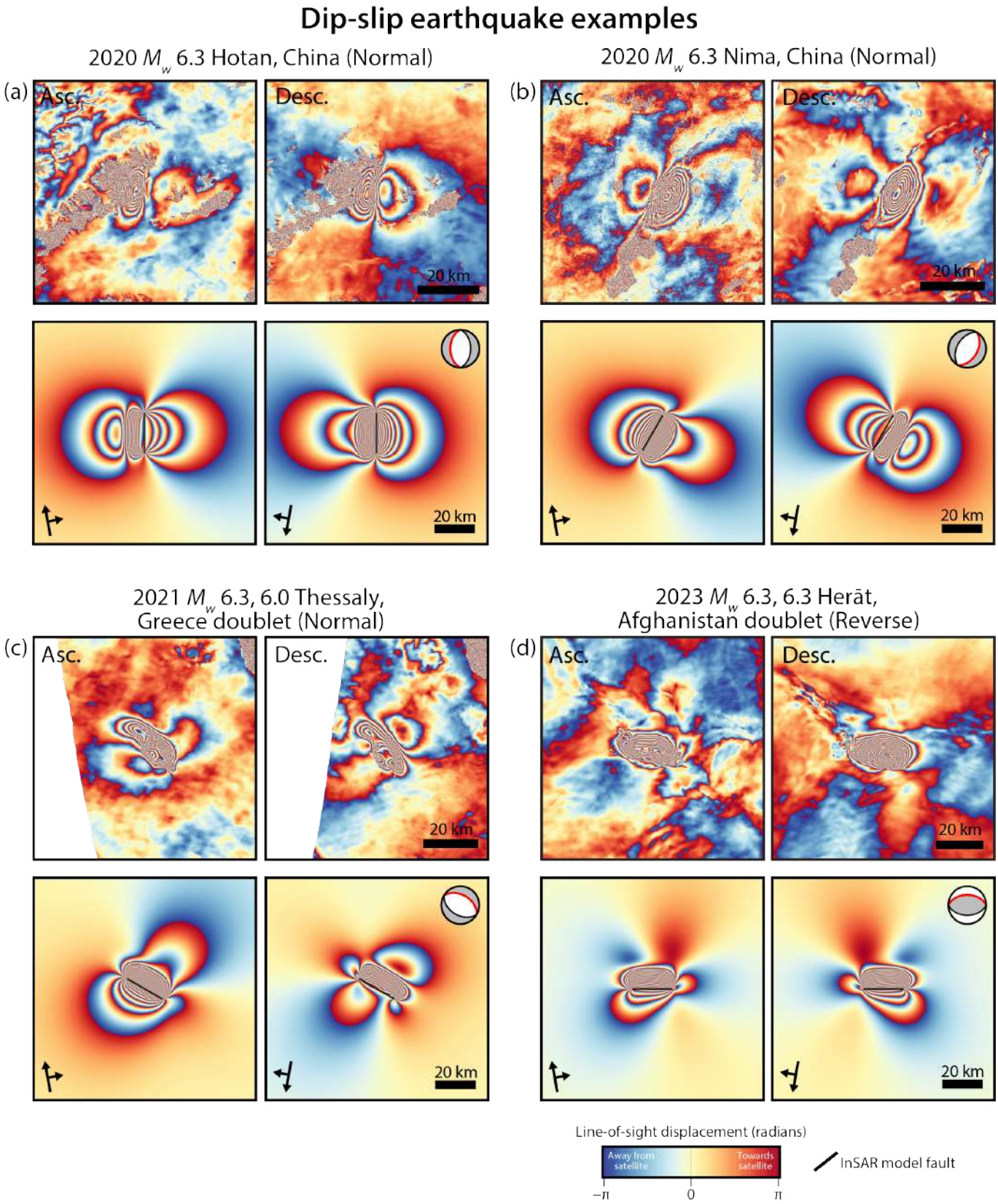

Figure 22 Comparisons between real dip-slip earthquake deformation interferograms (top rows) and our closest-matching lookbook models (bottom rows) for the (a) 2020 $\mathrm{M_w}$ 6.3 Hotan, China, (b) 2020 $\mathrm{M_w}$ 6.3 Nima, China, (c) 2021 $\mathrm{M_w}$ 6.3, 6.0 Thessaly, Greece (doublet), and (d) 2023 $\mathrm{M_w}$ 6.3, 6.3 Herāt, Afghanistan (doublet) earthquakes (see Table 2 for earthquake details). Left and right columns are ascending and descending interferograms, respectively. Thick black lines indicate our model faults and conjugate arrows denote the satellite azimuth and line-of-sight. The beach ball is the earthquake focal mechanism of our InSAR model, with the fault plane outlined in red.

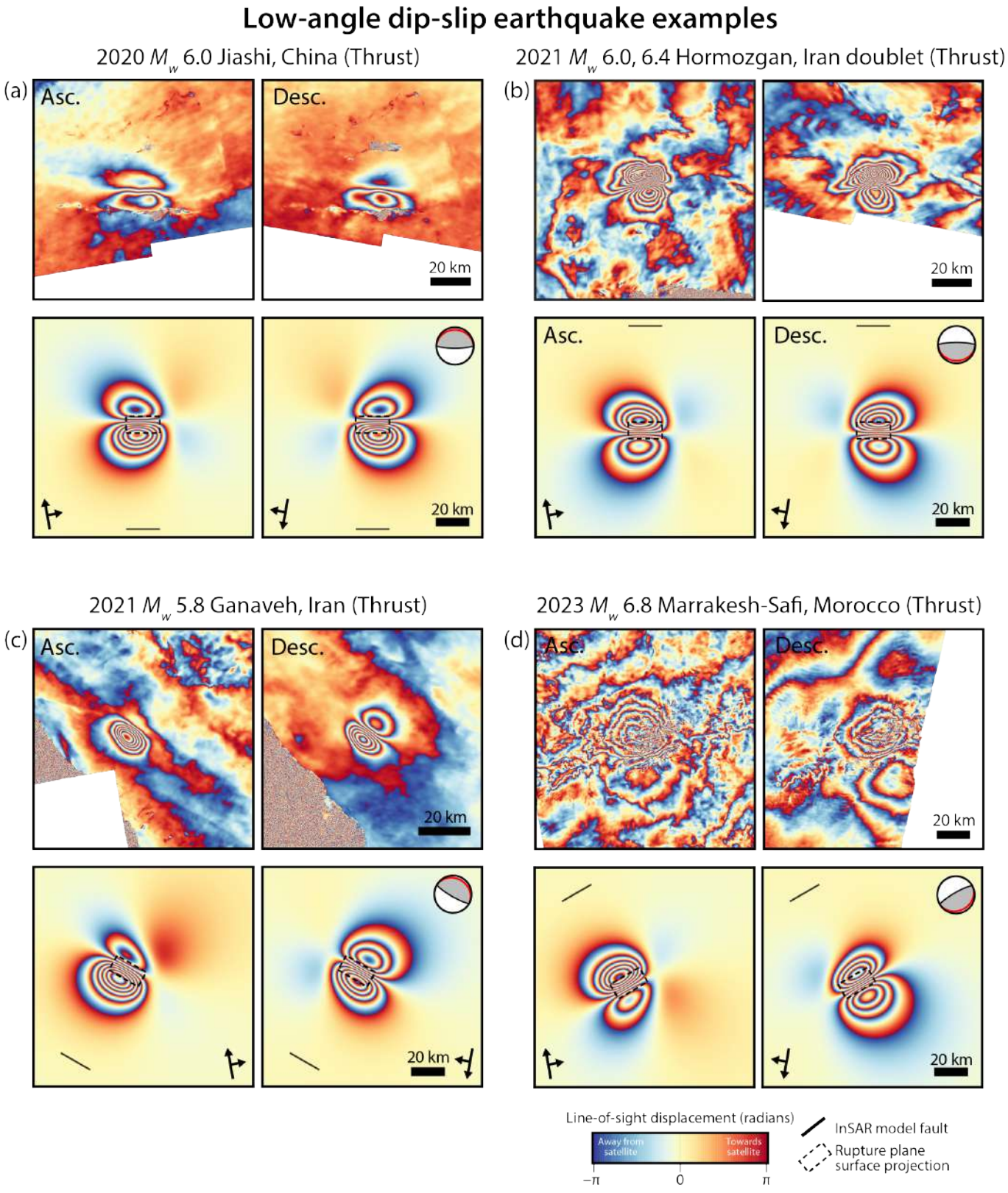

Figure 23 Comparisons between real low-angle thrust earthquake deformation interferograms (top rows) and our closest-matching lookbook models (bottom rows) for the (a) 2020 $\mathrm{M_w}$ 6.0 Jiashi, China, (b) 2021 $\mathrm{M_w}$ 6.0, 6.4 Hormozgan, Iran (doublet), (c) 2021 $\mathrm{M_w}$ 5.8 Ganaveh, Iran, and (d) 2023 $\mathrm{M_w}$ 6.8 Marrakesh-Safi, Morocco earthquakes (see Table 2 for earthquake details). Left and right columns are ascending and descending interferograms, respectively. Thick black lines indicate our model faults and conjugate arrows denote the satellite azimuth and line-of-sight. The beach ball is the earthquake focal mechanism of our InSAR model, with the fault plane outlined in red.

InSAR and whose deformation patterns overlap and merge. Ascending and descending interferograms each exhibit a simple two-lobed shape, with the opposite displacement sense to the Jiashi example: the northern lobes contain displacements towards the satellite and the southern lobes contain less than half those displacements away from the satellite (Figure 23b). This pattern is characteristic of an E-striking (S-dipping) low-angle thrust fault. However, North-side-up dip-slip on the conjugate, subvertical, W-striking nodal plane (a configuration at odds with Andersonian mechanics and beyond the scope of our lookbook) would generate a similar surface deformation pattern, and cannot be ruled out on the basis of InSAR alone. This is reflected in disagreements over the choice of fault plane amongst three, published studies (Golshadi et al., 2023; Rezapour and Jamalreyhani, 2023; Namdarsehat et al., 2024).

The 2021 M_w 5.8 Ganaveh, Iran earthquake, also in the frontal Zagros, exhibits a principal, NW-trending deformation lobe with displacements towards both ascending and descending satellites (Figure 23c). The descending interferogram contains a secondary, northeastern lobe moving away from the satellite; the equivalent lobe in the ascending interferogram is mostly obscured by atmospheric noise. The pattern is consistent with a WNW-striking low-angle thrust fault, in agreement with two published InSAR modelling studies (Jafari et al., 2023; Jamalreyhani et al., 2023).

Interferograms for the 2023 M_w 6.8 Marrakesh-Safi, Morocco earthquake in the Atlas mountains contain more short-wavelength atmospheric noise than those of our other low-angle thrust examples, but a pair of long-wavelength deformation lobes can still be made out (Figure 23d). The northern lobe contains displacements towards both ascending and descending satellites but is broader in the ascending interferogram; the southern lobe has the opposite displacement sense but is broader in the descending case. This pattern is consistent with the ENE-striking (SSE-dipping) low-angle thrust model from our lookbook. Modelling of the InSAR by Cheloni et al. (2024) supported a significant right-lateral component on a buried (∼15–30 km), 22°, SSW-dipping fault plane. While there are significant strike and rake discrepancies between our low-angle thrust forward model and Cheloni et al.'s oblique-slip inverse model, both involve NW-directed slip vectors on gently dipping planes, explaining the similarity of deformation. The visual match to our closest oblique-slip lookbook solution—the 120° strike model in Figure 15—is poorer owing to its much shallower depth.

5.4 Oblique-slip examples

The 15 December 2019 M_w 6.8 Mindanao, Philippines earthquake—the last and largest of a sequence of four major events in late 2019 along the southern Cotabato fault system—produced two lobes in a skewed butterfly pattern in the ascending interferogram and a more complicated three-lobed shape in the descending interferogram, a distinction diagnostic of oblique-slip faulting (Figure 24a). A distinct NW–SE discontinuity separating lobes in both satellite geometries hints at the fault orientation, and our NNW-striking, steep left-lateral/reverse faulting interferograms match the deformation well (Figure 20). This inference is supported by an inverse model by Li et al. (2020).

The 2021 M_w 6.7 Khövsgöl, Mongolia earthquake also shows two lobes in the ascending ALOS-2 interferogram (in which fringes represent ∼12 cm increments of LOS displacement) and three lobes in the descending one (Figure 24b). The decorrelated region in the SE of the interferograms is Khövsgöl Lake, obscuring much but not all of the southeastern lobe. Altogether, the Khövsgöl interferograms resemble those of the Mindanao earthquake but with opposite sense of motion, matching the NNW-striking right-lateral/normal earthquake in our lookbook (Figure 20). This is in broad agreement with published inverse models, suggesting strike, dip, and rake values of 340° to 345°, 42° to 59°, and –116° to –146°, respectively (Kim and Han, 2023; He et al., 2022; Liu et al., 2021b, 2022).

The 2024 M_w 7.0 Wushi, China earthquake in the southwestern Tian Shan generated a butterfly-shaped deformation pattern in the ascending interferogram and a three-lobed shape in the descending one (Figure 24c). In general, the satellite look vector that yields the simpler, butterfly pattern gives away the fault orientation—a clear ENE–WSW lineament in this case. We utilize the fixed strike (variable rake) model interferograms at 60° and 240° (Figures S2c and S2i) to confirm a match with a WSW-striking, steep left-lateral/reverse faulting interferogram. This is consistent both with automated USGS ANSS ComCat and GCMT moment tensors and with the kinematics of the WSW-striking Maidan fault, which likely hosted the earthquake (Wu et al., 2019; Guo et al., 2024).

Lastly, the 2020 M_w 6.5 Monte Cristo Range earthquake in the Mina deflection zone, part of the Walker Lane of California-Nevada, produced two deformation lobes in the ascending interferogram and three in the descending one (Figure 24d). Similar to the Wushi earthquake, the simpler butterfly pattern in the ascending interferogram suggests faulting parallel to the ENE look vector, and our lookbook summary (Figure 20) supports ENE-striking, left-lateral/normal faulting (rake = −45°). However, published InSAR inverse models reveal a more complicated two-fault geometry, with a shorter left-lateral/normal segment in the west crossing a longer left-lateral segment in the east (e.g., Sethanant et al., 2023; Li et al., 2021b; Liu et al., 2021a; Cui et al., 2021). This is reflected in the southern pair of lobes in the descending interferogram, which have different shapes to those in the lookbook (a squatter SW lobe and an elongate SE lobe).

6 Conclusions

This lookbook is the first systematic exploration of how InSAR surface deformation patterns evolve with varying strike and rake angles. Through its comprehensive atlas of ascending- and descending-track model interferograms, the lookbook provides an illustrated guide to estimating earthquake source mechanisms from InSAR data without the need for sophisticated inverse mod-

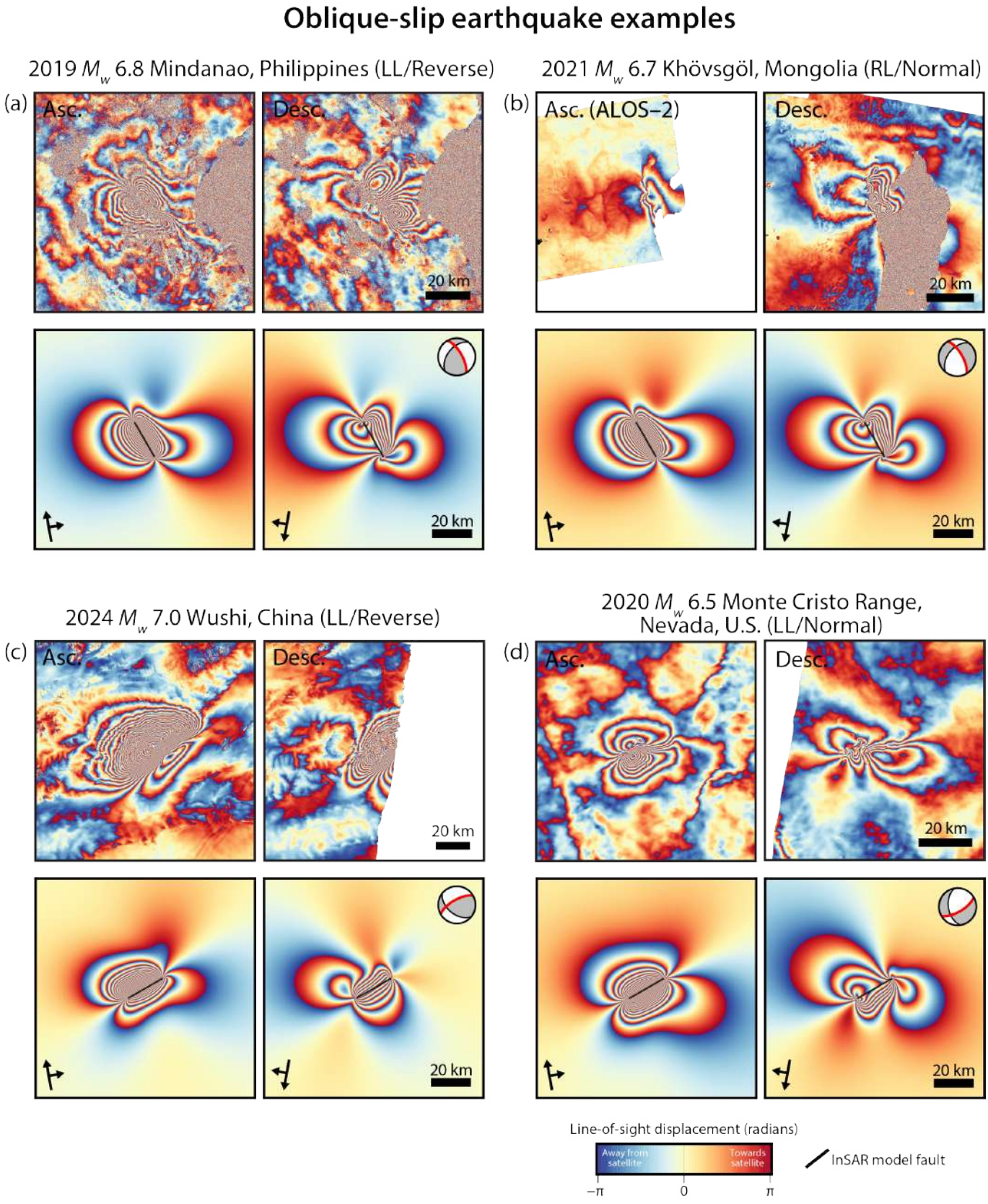

Figure 24 Comparisons between real oblique-slip earthquake deformation interferograms (top rows) and our closest-matching lookbook models (bottom rows) for the (a) 2019 $\mathrm{M_w}$ 6.8 Mindanao, Philippines (b) 2021 $\mathrm{M_w}$ 6.7 Khövsgöl, Mongolia, (c) 2024 $\mathrm{M_w}$ 7.0 Wushi, China, and (d) 2020 $\mathrm{M_w}$ 6.5 Monte Cristo Range, USA earthquakes (see Table 2 for earthquake details). Left and right columns are ascending and descending interferograms, respectively. For the Khövsgöl earthquake, the ALOS-2 ascending interferogram half-wavelength is ∼12 cm (panel b, top left). Thick black lines indicate our model faults and conjugate arrows denote the satellite azimuth and line-of-sight. The beach ball is the earthquake focal mechanism of our InSAR model, with the fault plane outlined in red.

elling. With growing numbers of InSAR satellites and increased availability of pre-processed imagery, this resource will be useful for rapid assessment of coseismic interferograms following large, onshore earthquakes.

Data and code availability

Displacement fields and forward model interferograms were generated using Oksar software provided by the Centre for Observation and Modelling of Earthquakes, Volcanoes and Tectonics (COMET). For the earthquakes plotted in Figures 21–24, Sentinel-1 interferograms were downloaded from the COMET LiCSAR portal (https://comet.nerc.ac.uk/comet-lics-portal-earthquake-event/, last accessed on May 31, 2024) while Envisat and ALOS-2 interferograms for the 2003 Bam and 2021 Khövsgöl earthquakes were kindly provided by Dr. Gareth Funning (Funning et al., 2005) and Dr. Hyangsun Han (Kim and Han, 2023), respectively. We used the interferogram color scale developed by Watson et al. (2023) and obtained from https://github.com/comet-licsar/licsar_proc/blob/main/misc/pha.cpt (last accessed May 31, 2024). Figures were plotted using the Generic Mapping Tools version 6 (Wessel et al., 2019). Scripts and parameter input files used to generate all lookbook interferograms and figures are provided in https://github.com/isethanant/insar_lookbook.

Competing interests

The authors have no competing interests.

Acknowledgements

Our lookbook was inspired in part by Gareth Funning and Rowan Cockett's Visible Earthquakes interactive website (Funning and Cockett, 2012). Work was supported by an NSERC Discovery Grant and Canada Research Chair to E.N., and the Diana and Martin Hocking Graduate Scholarship (University of Victoria) to I.S. We thank Louise Gall for help with formatting in LaTeX, and Kelin Wang and Yijie Zhu for discussing model implementations. We thank Austin Elliott and an anonymous reviewer for feedback that greatly improved the clarity, comprehensiveness, and presentation of the lookbook.

References

Barnhart, W. D., Hayes, G. P., and Wald, D. J. Global Earthquake Response with Imaging Geodesy: Recent Examples from the USGS NEIC. *Remote Sensing*, 11(11):1357, June 2019. doi: 10.3390/rs11111357.

Berberian, M., Jackson, J. A., Fielding, E., Parsons, B. E., Priestley, K., Qorashi, M., Talebian, M., Walker, R., Wright, T. J., and Baker, C. The 1998 March 14 Fandoqa earthquake (M_w 6.6) in Kerman province, southeast Iran: re-rupture of the 1981 Sirch earthquake fault, triggering of slip on adjacent thrusts and the active tectonics of the Gowk fault zone. *Geophysical Journal International*, 146(2):371–398, Aug. 2001. doi: 10.1046/j.1365-246x.2001.01459.x.

Biggs, J., Bergman, E., Emmerson, B., Funning, G. J., Jackson, J., Parsons, B., and Wright, T. J. Fault identification for buried strike-slip earthquakes using InSAR: The 1994 and 2004 Al Hoceima, Morocco earthquakes. *Geophysical Journal International*, 166(3):1347–1362, Sept. 2006. doi: 10.1111/j.1365-246x.2006.03071.x.

Bürgmann, R., Rosen, P. A., and Fielding, E. J. Synthetic Aperture Radar Interferometry to Measure Earth's Surface Topography and Its Deformation. *Annual Review of Earth and Planetary Sciences*, 28(1):169–209, May 2000. doi: 10.1146/annurev.earth.28.1.169.

Cheloni, D., Famiglietti, N. A., Tolomei, C., Caputo, R., and Vicari, A. The 8 September 2023, M_W 6.8, Morocco Earthquake: A Deep Transpressive Faulting Along the Active High Atlas Mountain Belt. *Geophysical Research Letters*, 51(2), Jan. 2024. doi: 10.1029/2023gl106992.

Collettini, C. and Sibson, R. H. Normal faults, normal friction? *Geology*, 29(10):927, 2001. doi: 10.1130/0091-7613(2001)029<0927:nfnf>2.0.co;2.

Cui, Y., Ma, Z., Aoki, Y., Liu, J., Yue, D., Hu, J., Zhou, C., and Li, Z. Refining slip distribution in moderate earthquakes using Sentinel-1 burst overlap interferometry: a case study over 2020 May 15 M_w 6.5 Monte Cristo Range Earthquake. *Geophysical Journal International*, 229(1):472–486, Dec. 2021. doi: 10.1093/gji/ggab492.

Delbridge, B. G., Bürgmann, R., Fielding, E., Hensley, S., and Schulz, W. H. Three-dimensional surface deformation derived from airborne interferometric UAVSAR: Application to the Slumgullion Landslide. *Journal of Geophysical Research: Solid Earth*, 121(5):3951–3977, May 2016. doi: 10.1002/2015jb012559.

Dolan, J. F. and Haravitch, B. D. How well do surface slip measurements track slip at depth in large strike-slip earthquakes? The importance of fault structural maturity in controlling on-fault slip versus off-fault surface deformation. *Earth and Planetary Science Letters*, 388:38–47, Feb. 2014. doi: 10.1016/j.epsl.2013.11.043.

Elliott, J., Walters, R., and Wright, T. The role of space-based observation in understanding and responding to active tectonics and earthquakes. *Nature Communications*, 7(1), Dec. 2016. doi: 10.1038/ncomms13844.

Elliott, J. R., Parsons, B., Jackson, J. A., Shan, X., Sloan, R. A., and Walker, R. T. Depth segmentation of the seismogenic continental crust: The 2008 and 2009 Qaidam earthquakes. *Geophysical Research Letters*, 38(6), Mar. 2011. doi: 10.1029/2011gl046897.

Elliott, J. R., Nissen, E. K., England, P. C., Jackson, J. A., Lamb, S., Li, Z., Oehlers, M., and Parsons, B. Slip in the 2010-2011 Canterbury earthquakes, New Zealand. *Journal of Geophysical Research: Solid Earth*, 117(B3), Mar. 2012. doi: 10.1029/2011jb008868.

Elliott, J. R., Elliott, A. J., Hooper, A., Larsen, Y., Marinkovic, P., and Wright, T. J. Earthquake monitoring gets boost from new satellite. *Eos*, 96, Feb. 2015. doi: 10.1029/2015eo023967.

European Space Agency. Sentinel-1, S1 Mission. https://sentiwiki.copernicus.eu/web/s1-mission. Accessed on March 6, 2025.

Fang, J., Houseman, G. A., Wright, T. J., Evans, L. A., Craig, T. J., Elliott, J. R., and Hooper, A. The Dynamics of the India-Eurasia Collision: Faulted Viscous Continuum Models Constrained by High-Resolution Sentinel-1 InSAR and GNSS Velocities. *Journal of Geophysical Research: Solid Earth*, 129(6), June 2024. doi: 10.1029/2023jb028571.

Fialko, Y., Sandwell, D., Simons, M., and Rosen, P. Three-dimensional deformation caused by the Bam, Iran, earthquake and the origin of shallow slip deficit. *Nature*, 435(7040):295–299, May 2005. doi: 10.1038/nature03425.

Fielding, E. J., Talebian, M., Rosen, P. A., Nazari, H., Jackson, J. A., Ghorashi, M., and Walker, R. Surface ruptures and building

damage of the 2003 Bam, Iran, earthquake mapped by satellite synthetic aperture radar interferometric correlation. *Journal of Geophysical Research: Solid Earth*, 110(B3), Mar. 2005. doi: 10.1029/2004jb003299.

Funning, G. J. and Cockett, R. Visible Earthquakes: a web-based tool for visualizing and modeling InSAR earthquake data. In *AGU Fall Meeting Abstracts*, volume 2012, pages ED43E–06, Dec. 2012.

Funning, G. J. and Garcia, A. A systematic study of earthquake detectability using Sentinel-1 Interferometric Wide-Swath data. *Geophysical Journal International*, 216(1):332–349, Jan. 2019. doi: 10.1093/gji/ggy42610.31223/osf.io/9wg8s.

Funning, G. J., Parsons, B., Wright, T. J., Jackson, J. A., and Fielding, E. J. Surface displacements and source parameters of the 2003 Bam (Iran) earthquake from Envisat advanced synthetic aperture radar imagery. *Journal of Geophysical Research: Solid Earth*, 110(B9), Sept. 2005. doi: 10.1029/2004jb003338.

Gabriel, A. K., Goldstein, R. M., and Zebker, H. A. Mapping small evaluation changes over large areas: Differential radar interferometry. *Journal of Geophysical Research: Solid Earth*, 94(B7): 9183–9191, July 1989. doi: 10.1029/jb094ib07p09183.

Gao, H., Liao, M., Liang, X., Feng, G., and Wang, G. Coseismic and Postseismic Fault Kinematics of the July 22, 2020, Nima (Tibet) Ms6.6 Earthquake: Implications of the Forming Mechanism of the Active N-S-Trending Grabens in Qiangtang, Tibet. *Tectonics*, 41(3), Feb. 2022. doi: 10.1029/2021tc006949.

Gaudreau, É., Hollingsworth, J., Nissen, E., and Funning, G. J. Complex 3-D Surface Deformation in the 1971 San Fernando, California Earthquake Reveals Static and Dynamic Controls on Off-Fault Deformation. *Journal of Geophysical Research: Solid Earth*, 128(3):e2022JB024985, Mar. 2023. doi: 10.1029/2022JB024985.

Golshadi, Z., Famiglietti, N. A., Caputo, R., SoltaniMoghadam, S., Karimzadeh, S., Memmolo, A., Falco, L., and Vicari, A. Contemporaneous Thick- and Thin-Skinned Seismotectonics in the External Zagros: The Case of the 2021 Fin Doublet, Iran. *Remote Sensing*, 15(12):2981, June 2023. doi: 10.3390/rs15122981.

Guo, N., Wu, Y., Zhu, S., and Chen, C. Coseismic deformation and interseismic strain accumulation of the 2024 MS 7.1 Wushi earthquake in Xinjiang, China. *Advances in Space Research*, 74(4): 1586–1594, Aug. 2024. doi: 10.1016/j.asr.2024.05.028.

Hamling, I. J., Hreinsdóttir, S., Clark, K., Elliott, J., Liang, C., Fielding, E., Litchfield, N., Villamor, P., Wallace, L., Wright, T. J., D'Anastasio, E., Bannister, S., Burbidge, D., Denys, P., Gentle, P., Howarth, J., Mueller, C., Palmer, N., Pearson, C., Power, W., Barnes, P., Barrell, D. J. A., Van Dissen, R., Langridge, R., Little, T., Nicol, A., Pettinga, J., Rowland, J., and Stirling, M. Complex multifault rupture during the 2016 M_w 7.8 Kaikōura earthquake, New Zealand. *Science*, 356(6334), Apr. 2017. doi: 10.1126/science.aam7194.

He, Y., Wang, T., and Zhao, L. The 2021 Mw6.7 Lake Hovsgol (Mongolia) Earthquake: Irregular Normal Faulting with Slip Partitioning Controlled by an Adjacent Strike-Slip Fault. *Remote Sensing*, 14(18):4553, Sept. 2022. doi: 10.3390/rs14184553.

Huang, M., Fielding, E. J., Liang, C., Milillo, P., Bekaert, D., Dreger, D., and Salzer, J. Coseismic deformation and triggered landslides of the 2016 M_w 6.2 Amatrice earthquake in Italy. *Geophysical Research Letters*, 44(3):1266–1274, Feb. 2017. doi: 10.1002/2016gl071687.

Institute of Electrical and Electronics Engineers. IEEE Standard Letter Designations for Radar-Frequency Bands. *IEEE Std 521-2019 (Revision of IEEE Std 521-2002)*, 2020.

Ishitsuka, K., Tsuji, T., and Matsuoka, T. Detection and mapping of soil liquefaction in the 2011 Tohoku earthquake using SAR interferometry. *Earth, Planets and Space*, 64(12):1267–1276, Dec. 2012. doi: 10.5047/eps.2012.11.002.

Jafari, M., Aflaki, M., Mousavi, Z., Walpersdorf, A., and Motaghi, K. Coseismic and post-seismic characteristics of the 2021 Ganaveh earthquake along the Zagros foredeep fault based on InSAR data. *Geophysical Journal International*, 234(2):1125–1142, Mar. 2023. doi: 10.1093/gji/ggad127.

Jamalreyhani, M., Pousse-Beltran, L., Hassanzadeh, M., Sadat Arabi, S., A. Bergman, E., Shamszadeh, A., Arvin, S., Fariborzi, N., and Songhori, A. Co-seismic slip of the 18 April 2021 Mw 5.9 Genaveh earthquake in the South Dezful Embayment of Zagros (Iran) and its aftershock sequence. *Seismica*, 2(1), May 2023. doi: 10.26443/seismica.v2i1.246.

Karasözen, E., Nissen, E., Büyükakpınar, P., Cambaz, M. D., Kahraman, M., Kalkan Ertan, E., Abgarmi, B., Bergman, E., Ghods, A., and Özacar, A. A. The 2017 July 20 M_w 6.6 Bodrum-Kos earthquake illuminates active faulting in the Gulf of Gökova, SW Turkey. *Geophysical Journal International*, 214(1):185–199, Mar. 2018. doi: 10.1093/gji/ggy114.

Kennedy, J., Anderson, R., Biessel, R., Chase, T., Ellis, O., Fairbanks, K., Fleming, C., Horn, W., Johnston, A., Kristenson, H., Logan, T., Meyer, F., Miller, R., Rine, J., Showalter, C., Short, G., Zhu, J., and Player, A. Skip the Processing: On Demand Analysis-Ready InSAR from ASF. In *AGU Fall Meeting Abstracts*, volume 2021, pages G45B–0395, Dec. 2021.

Kim, T. and Han, H. Coseismic displacement fields and the slip mechanism of the 2021 Mw 6.7 Hovsgol earthquake in Mongolia constrained by Sentinel-1 and ALOS-2 InSAR. *GIScience & Remote Sensing*, 60(1), Feb. 2023. doi: 10.1080/15481603.2023.2180026.

Lazecký, M., Spaans, K., González, P. J., Maghsoudi, Y., Morishita, Y., Albino, F., Elliott, J., Greenall, N., Hatton, E., Hooper, A., Juncu, D., McDougall, A., Walters, R. J., Watson, C. S., Weiss, J. R., and Wright, T. J. LiCSAR: An Automatic InSAR Tool for Measuring and Monitoring Tectonic and Volcanic Activity. *Remote Sensing*, 12 (15):2430, July 2020. doi: 10.3390/rs12152430.

Li, B., Li, Y., Jiang, W., Su, Z., and Shen, W. Conjugate ruptures and seismotectonic implications of the 2019 Mindanao earthquake sequence inferred from Sentinel-1 InSAR data. *International Journal of Applied Earth Observation and Geoinformation*, 90:102127, Aug. 2020. doi: 10.1016/j.jag.2020.102127.

Li, K., Li, Y., Tapponnier, P., Xu, X., Li, D., and He, Z. Joint InSAR and Field Constraints on Faulting During the Mw 6.4, July 23, 2020, Nima/Rongma Earthquake in Central Tibet. *Journal of Geophysical Research: Solid Earth*, 126(9), Aug. 2021a. doi: 10.1029/2021jb022212.

Li, K., Tapponnier, P., Xu, X., and Kang, W. The 2022, Ms 6.9 Menyuan earthquake: Surface rupture, Paleozoic suture reactivation, slip-rate and seismic gap along the Haiyuan fault system, NE Tibet. *Earth and Planetary Science Letters*, 622:118412, Nov. 2023. doi: 10.1016/j.epsl.2023.118412.

Li, S., Tao, T., Chen, Y., He, P., Gao, F., Qu, X., and Zhu, Y. Geodetic Observation and Modeling of the Coseismic and Postseismic Deformations Associated With the 2020 Mw 6.5 Monte Cristo Earthquake. *Earth and Space Science*, 8(6), June 2021b. doi: 10.1029/2021ea001696.

Liu, C., Lay, T., Pollitz, F. F., Xu, J., and Xiong, X. Seismic and Geodetic Analysis of Rupture Characteristics of the 2020 M_w 6.5 Monte Cristo Range, Nevada, Earthquake. *Bulletin of the Seismological Society of America*, 111(6):3226–3236, July 2021a. doi: 10.1785/0120200327.

Liu, G., Qiao, X., Yu, P., Zhou, Y., Zhao, B., and Xiong, W. Rupture Kinematics of the 11 January 2021 Mw 6.7 Hovsgol, Mongolia, Earthquake and Implications in the Western Baikal Rift

Zone. *Seismological Research Letters*, 92(6):3318–3326, July 2021b. doi: 10.1785/0220210061.

Liu, X., Xu, W., Radziminovich, N. A., Fang, N., and Xie, L. Transtensional coseismic fault slip of the 2021 Mw 6.7 Turt Earthquake and heterogeneous tectonic stress surrounding the Hovsgol Basin, Northwest Mongolia. *Tectonophysics*, 836:229407, Aug. 2022. doi: 10.1016/j.tecto.2022.229407.

Liu, X., Xia, T., Liu-Zeng, J., Deng, D., Jia, Z., Wang, P., Yu, P., and Wang, W. Coseismic and early postseismic deformation of the 2020 Nima Mw 6.4 earthquake, central Tibet, from InSAR and GNSS observations. *Frontiers in Earth Science*, 10, Jan. 2023. doi: 10.3389/feart.2022.1012773.

Liu, Z., Li, Z., Yu, C., Zhang, X., and Peng, J. Stress triggering and future seismic hazards implied by four large earthquakes in the Pamir from 2015 to 2023 revealed by Sentinel-1 radar interferometry. *Geophysical Journal International*, 237(2):887–901, Mar. 2024. doi: 10.1093/gji/ggae079.

Lohman, R. B. and Barnhart, W. D. Evaluation of earthquake triggering during the 2005-2008 earthquake sequence on Qeshm Island, Iran. *Journal of Geophysical Research: Solid Earth*, 115 (B12), Dec. 2010. doi: 10.1029/2010jb007710.

Magen, Y., Ziv, A., Inbal, A., Baer, G., and Hollingsworth, J. Fault Rerupture during the July 2019 Ridgecrest Earthquake Pair from Joint Slip Inversion of InSAR, Optical Imagery, and GPS. *Bulletin of the Seismological Society of America*, 110(4):1627–1643, June 2020. doi: 10.1785/0120200024.

Mai, P. M. and Thingbaijam, K. K. S. SRCMOD: An Online Database of Finite-Fault Rupture Models. *Seismological Research Letters*, 85(6):1348–1357, Oct. 2014. doi: 10.1785/0220140077.

Massonnet, D. and Feigl, K. L. Radar interferometry and its application to changes in the Earth's surface. *Reviews of Geophysics*, 36(4):441–500, Nov. 1998. doi: 10.1029/97rg03139.

Massonnet, D., Rossi, M., Carmona, C., Adragna, F., Peltzer, G., Feigl, K., and Rabaute, T. The displacement field of the Landers earthquake mapped by radar interferometry. *Nature*, 364 (6433):138–142, July 1993. doi: 10.1038/364138a0.

Meyer, F. J., Arko, S. A., Hogenson, K., McAlpin, D. B., and Whitley, M. A. A Cloud-Based System for Automatic Hazard Monitoring from Sentinel-1 SAR Data. In *AGU Fall Meeting Abstracts*, volume 2017, pages G33A–03, Dec. 2017.

Middleton, T. A. and Copley, A. Constraining fault friction by reexamining earthquake nodal plane dips. *Geophysical Journal International*, 196(2):671–680, Nov. 2013. doi: 10.1093/gji/ggt427.

Milliner, C. W. D., Dolan, J. F., Hollingsworth, J., Leprince, S., Ayoub, F., and Sammis, C. G. Quantifying near-field and off-fault deformation patterns of the 1992 M_w 7.3 Landers earthquake. *Geochemistry, Geophysics, Geosystems*, 16(5):1577–1598, May 2015. doi: 10.1002/2014gc005693.

Namdarsehat, P., Milczarek, W., Bugajska-Jędraszek, N., Motavalli-Anbaran, S.-H., and Khaledzadeh, M. Uncovering a Seismogenic Fault in Southern Iran through Co-Seismic Deformation of the Mw 6.1 Doublet Earthquake of 14 November 2021. *Remote Sensing*, 16(13):2318, June 2024. doi: 10.3390/rs16132318.

Nissen, E., Elliott, J. R., Sloan, R. A., Craig, T. J., Funning, G. J., Hutko, A., Parsons, B. E., and Wright, T. J. Limitations of rupture forecasting exposed by instantaneously triggered earthquake doublet. *Nature Geoscience*, 9(4):330–336, Feb. 2016. doi: 10.1038/ngeo2653.

Nissen, E., Cambaz, M. D., Gaudreau, É., Howell, A., Karasözen, E., and Savidge, E. A reappraisal of active tectonics along the Fethiye-Burdur trend, southwestern Turkey. *Geophysical Journal International*, 230(2):1030–1051, Aug. 2022. doi: 10.1093/gji/ggac09610.31223/x5zc99.

Okada, Y. Surface deformation due to shear and tensile faults in a half-space. *Bulletin of the Seismological Society of America*, 75 (4):1135–1154, Aug. 1985. doi: 10.1785/bssa0750041135.

Owen, S. E., Hua, H., Rosen, P. A., Agram, P. S., Webb, F., Simons, M., Yun, S. H., Sacco, G. F., Liu, Z., Fielding, E. J., Lundgren, P., and Moore, A. W. The Advanced Rapid Imaging and Analysis (ARIA) Project: Providing Standard and On-Demand SAR products for Hazard Science and Hazard Response. In *AGU Fall Meeting Abstracts*, volume 2017, pages IN53B–0089, Dec. 2017.

Rezapour, M. and Jamalreyhani, M. R. Source fault analyses from InSAR data and aftershocks for the Fin doublet earthquakes on 14 November 2021 in Hormozgan province, South Iran. *Journal of the Earth and Space Physics*, 48(4):87–97, 2023. doi: 10.22059/jesphys.2022.337959.1007399.

Rosen, P., Hensley, S., Joughin, I., Li, F., Madsen, S., Rodriguez, E., and Goldstein, R. Synthetic aperture radar interferometry. *Proceedings of the IEEE*, 88(3):333–382, Mar. 2000. doi: 10.1109/5.838084.

Scott, C., Champenois, J., Klinger, Y., Nissen, E., Maruyama, T., Chiba, T., and Arrowsmith, R. The 2016 M7 Kumamoto, Japan, Earthquake Slip Field Derived From a Joint Inversion of Differential Lidar Topography, Optical Correlation, and InSAR Surface Displacements. *Geophysical Research Letters*, 46(12): 6341–6351, June 2019. doi: 10.1029/2019gl082202.

Sethanant, I., Nissen, E., Pousse-Beltran, L., Bergman, E., and Pierce, I. The 2020 M_w 6.5 Monte Cristo Range, Nevada, Earthquake: Anatomy of a Crossing-Fault Rupture through a Region of Highly Distributed Deformation. *Bulletin of the Seismological Society of America*, 113(3):948–975, Mar. 2023. doi: 10.1785/0120220166.

Shi, Y., Wang, Y., and Bian, Y. Coseismic Source Model of the February 2023 Mw 6.8 Tajikistan Earthquake from Sentinel-1A InSAR Observations and Its Associated Earthquake Hazard. *Remote Sensing*, 15(12):3010, June 2023. doi: 10.3390/rs15123010.

Talebian, M., Biggs, J., Bolourchi, M., Copley, A., Ghassemi, A., Ghorashi, M., Hollingsworth, J., Jackson, J., Nissen, E., Oveisi, B., Parsons, B., Priestley, K., and Saiidi, A. The Dahuiyeh (Zarand) earthquake of 2005 February 22 in central Iran: reactivation of an intramountain reverse fault. *Geophysical Journal International*, 164(1):137–148, Jan. 2006. doi: 10.1111/j.1365-246x.2005.02839.x.

Tong, X., Sandwell, D. T., and Fialko, Y. Coseismic slip model of the 2008 Wenchuan earthquake derived from joint inversion of interferometric synthetic aperture radar, GPS, and field data. *Journal of Geophysical Research: Solid Earth*, 115(B4), Apr. 2010. doi: 10.1029/2009jb006625.

U.S. Geological Survey. Advanced National Seismic System (ANSS) Comprehensive Catalog of Earthquake Events and Products: Various, 2017. doi: 10.5066/F7MS3QZH.

Walker, R. and Jackson, J. Offset and evolution of the Gowk fault, S.E. Iran: a major intra-continental strike-slip system. *Journal of Structural Geology*, 24(11):1677–1698, Nov. 2002. doi: 10.1016/s0191-8141(01)00170-5.

Wan, Y., Shen, Z.-K., Bürgmann, R., Sun, J., and Wang, M. Fault geometry and slip distribution of the 2008 M_w 7.9 Wenchuan, China earthquake, inferred from GPS and InSAR measurements. *Geophysical Journal International*, 208(2):748–766, Nov. 2016. doi: 10.1093/gji/ggw421.

Wang, S., Nissen, E., Pousse-Beltran, L., Craig, T. J., Jiao, R., and Bergman, E. A. Structural controls on coseismic rupture revealed by the 2020 M_w 6.0 Jiashi earthquake (Kepingtag belt, SW Tian Shan, China). *Geophysical Journal International*, 230(3):1895–1910, Sept. 2022. doi: 10.1093/gji/ggac15910.31223/x58w4c.

Watson, C. S., Elliott, J. R., Ebmeier, S. K., Biggs, J., Albino, F., Brown, S. K., Burns, H., Hooper, A., Lazecký, M., Maghsoudi, Y., Rigby, R., , and Wright, T. J. Strategies for improving the communication of satellite-derived InSAR data for geohazards through the analysis of Twitter and online data portals. *Geoscience Communication*, 6(2):75–96, June 2023. doi: 10.5194/gc-6-75-2023.

Wei, S., Fielding, E., Leprince, S., Sladen, A., Avouac, J.-P., Helmberger, D., Hauksson, E., Chu, R., Simons, M., Hudnut, K., Herring, T., and Briggs, R. Superficial simplicity of the 2010 El Mayor-Cucapah earthquake of Baja California in Mexico. *Nature Geoscience*, 4(9):615–618, July 2011. doi: 10.1038/ngeo1213.

Wells, D. L. and Coppersmith, K. J. New empirical relationships among magnitude, rupture length, rupture width, rupture area, and surface displacement. *Bulletin of the Seismological Society of America*, 84(4):974–1002, Aug. 1994. doi: 10.1785/bssa0840040974.

Wessel, P., Luis, J. F., Uieda, L., Scharroo, R., Wobbe, F., Smith, W. H. F., and Tian, D. The Generic Mapping Tools Version 6. *Geochemistry, Geophysics, Geosystems*, 20(11):5556–5564, Nov. 2019. doi: 10.1029/2019gc008515.

Weston, J., Ferreira, A. M. G., and Funning, G. J. Global compilation of interferometric synthetic aperture radar earthquake source models: 1. Comparisons with seismic catalogs. *Journal of Geophysical Research*, 116(B8), Aug. 2011. doi: 10.1029/2010jb008131.

Weston, J., Ferreira, A. M., and Funning, G. J. Systematic comparisons of earthquake source models determined using InSAR and seismic data. *Tectonophysics*, 532–535:61–81, Apr. 2012. doi: 10.1016/j.tecto.2012.02.001.

Wright, T., Parsons, B., Jackson, J., Haynes, M., Fielding, E., England, P., and Clarke, P. Source parameters of the 1 October 1995 Dinar (Turkey) earthquake from SAR interferometry and seismic bodywave modelling. *Earth and Planetary Science Letters*, 172 (1–2):23–37, Oct. 1999. doi: 10.1016/s0012-821x(99)00186-7.

Wright, T. J., Elliott, J. R., Wang, H., and Ryder, I. Earthquake cycle deformation and the Moho: Implications for the rheology of continental lithosphere. *Tectonophysics*, 609:504–523, Dec. 2013. doi: 10.1016/j.tecto.2013.07.029.

Wu, C., Zheng, W., Zhang, P., Zhang, Z., Jia, Q., Yu, J., Zhang, H., Yao, Y., Liu, J., Han, G., and Chen, J. Oblique Thrust of the Maidan Fault and Late Quaternary Tectonic Deformation in the Southwestern Tian Shan, Northwestern China. *Tectonics*, 38(8): 2625–2645, Aug. 2019. doi: 10.1029/2018tc005248.

Xiong, W., Yu, P., Chen, W., Liu, G., Zhao, B., Nie, Z., and Qiao, X. The 2020 M_w 6.4 Petrinja earthquake: a dextral event with large coseismic slip highlights a complex fault system in northwestern Croatia. *Geophysical Journal International*, 228(3):1935–1945, Nov. 2021. doi: 10.1093/gji/ggab440.

Xu, X., Tong, X., Sandwell, D. T., Milliner, C. W., Dolan, J. F., Hollingsworth, J., Leprince, S., and Ayoub, F. Refining the shallow slip deficit. *Geophysical Journal International*, 204(3): 1843–1862, Feb. 2016. doi: 10.1093/gji/ggv563.

Xu, X., Sandwell, D. T., Ward, L. A., Milliner, C. W. D., Smith-Konter, B. R., Fang, P., and Bock, Y. Surface deformation associated with fractures near the 2019 Ridgecrest earthquake sequence. *Science*, 370(6516):605–608, Oct. 2020. doi: 10.1126/science.abd1690.

Yang, J., Xu, C., Wen, Y., and Xu, G. Complex Coseismic and Postseismic Faulting During the 2021 Northern Thessaly (Greece) Earthquake Sequence Illuminated by InSAR Observations. *Geophysical Research Letters*, 49(8), Apr. 2022. doi: 10.1029/2022gl098545.

Yu, C., Li, Z., Penna, N. T., and Crippa, P. Generic Atmospheric Correction Model for Interferometric Synthetic Aperture Radar Observations. *Journal of Geophysical Research: Solid Earth*, 123 (10):9202–9222, Oct. 2018. doi: 10.1029/2017jb015305.

Yu, J., Wang, D., Zhao, B., and Li, Q. Normal Faulting Movement During the 2020 Mw 6.4 Yutian Earthquake: A Shallow Rupture in NW Tibet Revealed by Geodetic Measurements. *Pure and Applied Geophysics*, 178(5):1563–1578, May 2021. doi: 10.1007/s00024-021-02735-w.

Zebker, H. and Villasenor, J. Decorrelation in interferometric radar echoes. *IEEE Transactions on Geoscience and Remote Sensing*, 30(5):950–959, 1992. doi: 10.1109/36.175330.

Zebker, H. A. and Lu, Y. Phase unwrapping algorithms for radar interferometry: residue-cut, least-squares, and synthesis algorithms. *Journal of the Optical Society of America A*, 15(3):586, Mar. 1998. doi: 10.1364/josaa.15.000586.

Zhang, Y., Shan, X., Gong, W., and Zhang, G. The ambiguous fault geometry derived from InSAR measurements of buried thrust earthquakes: a synthetic data based study. *Geophysical Journal International*, 225(3):1799–1811, Mar. 2021. doi: 10.1093/gji/ggab021.

Zhao, L., Nissen, E., Xu, W., Jamalreyhani, M., Bergman, E. A., Zhao, D., and Xie, L. Variable fault geometry controls the cascading 2023 Herat, Afghanistan multiplet sequence. *Communications Earth & Environment*, 6(1), Feb. 2025. doi: 10.1038/s43247-025-02113-7.

Zhu, C., Wang, C., Zhang, B., Qin, X., and Shan, X. Differential Interferometric Synthetic Aperture Radar data for more accurate earthquake catalogs. *Remote Sensing of Environment*, 266: 112690, Dec. 2021. doi: 10.1016/j.rse.2021.112690.

The article *The InSAR lookbook: an illustrated guide to earthquake deformation interferograms* © 2025 by Israporn Sethanant is licensed under CC BY 4.0.